Equatorial waves resolved by balloon-borne Global Navigation Satellite System Radio Occultation in the Strateole-2 Campaign

Bing Cao[1], Jennifer S. Haase[1], Michael J. Murphy[1], M. Joan Alexander[2], Martina Bramberger[2], and Albert Hertzog[3]

[1]Scripps Institution Oceanography, University of California San Diego, La Jolla, CA, USA
[2]Northwest Research Association, Boulder, CO, USA
[3]Laboratoire de Météorologie Dynamique, Sorbonne Université, École Polytechnique, CNRS, Palaiseau, France

Correspondence: Bing Cao (bic020@ucsd.edu)

Abstract. Current climate models have difficulty representing realistic wave-mean flow interactions, partly because the contribution from waves with fine-vertical scales is poorly known. There are few direct observations of these waves and most models have difficulty resolving them. This observational challenge cannot be addressed by satellite or sparse ground-based methods. The Strateole-2 long-duration stratospheric superpressure balloons that drift with the horizontal wind on constant

5 density surfaces provide a unique platform for wave observations across a broad range of spatial and temporal scales. For the first time, balloon-borne Global Navigation Satellite System (GNSS) radio occultation (RO) is used to provide high vertical resolution equatorial wave observations. By tracking navigation signal refractive delays from GPS satellites near the horizon, 40–50 temperature profiles were retrieved daily, from balloon flight altitude (∼20 km) down to 6–8 km altitude, forming an orthogonal pattern of observations over a broad area (±400–500 km) surrounding the flight track. The refractivity profiles

10 show an excellent agreement of better than 0.2 % with co-located radiosonde, spaceborne COSMIC-2 RO and reanalysis products. The 200–500 m vertical resolution and consecutive sampling in time and space make it possible to extract properties of Kelvin waves to shorter period gravity waves with vertical wavelengths as short as 2–3 km. A short dataset from the extra Galileo and GLONASS constellations demonstrates the feasibility to nearly double the sampling density in planned follow-on campaigns. The results will contribute to improved estimates of momentum forces for wave driving of the Quasi-biennial Os-

15 cillation (QBO) and improved QBO representation in models, and illustrate the importance of measuring intrinsic period in the Lagrangian reference frame.

Short Summary

Atmospheric waves that carry momentum from the tropospheric weather systems into the equatorial stratosphere modify the winds there. The 2019 Strateole-2 campaign launched long-duration stratospheric superpressure balloons to measure these

20 equatorial waves. We deployed a GPS receiver on one of the balloons to measure atmospheric temperature profiles beneath the balloon. Temperature variations in the retrieved profiles show planetary-scale waves with a 20 day period and 3–4 day period waves.

1 Introduction

The fine-vertical scales of atmospheric waves in the upper troposphere/lower stratosphere (UTLS) region create observational

25 challenges that cannot be addressed by either satellite or sparse ground-based observations (Vincent and Alexander, 2020). Modeling challenges persist due to the high resolution required to simulate waves and gaps in physical process understanding (Bushell et al., 2020). This work introduces the deployment of next-generation Global Navigation Satellite System (GNSS) receivers for Radio Occultation (RO) onboard long-duration stratospheric balloons to sample the equatorial wave field in three dimensions by retrieving a continuous sequence of temperature profiles on both sides of the balloon trajectory. The balloon-

30 borne RO observations from the Strateole-2 project enable investigations to quantify UTLS wave properties that are needed to improve model representations of wave driving of the quasi-biennial oscillation (QBO). They also enable investigations to determine the relationship of UTLS waves to thin cirrus clouds that can be used for improving their representation in models. This can be advanced by quantifying the global characteristics of waves that determine tropical cold point temperature variability for use in improving models of stratospheric dehydration (Kim and Alexander, 2015; Jensen et al., 2017).

35 Tropical waves in the UTLS have climate and weather impacts through their effects on cirrus clouds, stratospheric dehydration, and wave-driven circulation patterns. In particular, the QBO is a wave-driven circulation pattern with clear oscillations in the zonal mean zonal wind with a typical period of 27 months (Baldwin et al., 2001). It is the dominant mode of interannual lower stratospheric wind variability, affecting tropospheric variability through various teleconnections. The deposition of momentum by dissipation of tropical waves of a variety of scales is believed to be the main cause. However, current climate

40 models with limited resolution have difficulties producing a realistic QBO in the lower stratosphere due to unresolved small-scale waves (Richter et al., 2020), leading to uncertainty in the evolution of the QBO period in a changing climate. Direct observations that can inform the process of wave driving of the QBO are rare. The importance of QBO teleconnections to surface variability remains somewhat muted in forecast models compared to observations, a fact that may be closely related to model biases in QBO winds, particularly in the lowermost stratosphere (Bushell et al., 2020). The lowermost QBO winds

45 show evidence of weakening in recent decades (Kawatani and Hamilton, 2013) and models suggest the cause may be a gradual strengthening of the wave-driven stratospheric overturning circulation. However, this overturning cannot be directly observed, and the wave mean-flow interactions that drive the stratospheric circulation are plagued by uncertainties associated with the lack of knowledge of the wave properties. The two recent disruptions in the QBO, in 2015-2016 (Newman et al., 2016) and in 2019-2020 (Anstey et al., 2020a), where the normal progression of westerlies was interrupted, illustrate additional challenges

50 to predictability. Planetary-scale Rossby waves propagating from the Northern (in 2015) and Southern (in 2019) Hemisphere were the likely source of the disruption, and changes in wave-momentum flux from higher latitudes may become more common in the future (Anstey et al., 2020b).

GNSS RO has revolutionized the understanding of equatorial wave properties because its limb-sounding geometry resolves detailed vertical variations of temperature and atmospheric refractivity in the stratosphere (e.g., Tsuda et al., 2000; Randel

55 et al., 2003). The RO technique is based on the principle that the refractive bending and propagation delay of a transmitted navigation signal to a receiver on a Low Earth Orbiting (LEO) satellite is measured each time the LEO sets or rises relative

to GNSS satellites. The bending angle is inverted to produce an estimate of refractivity in a layered approximation of the Earth atmosphere, from which pressure and temperature can be derived (Kursinski et al., 1997; Fjeldbo and Eshleman, 1968). Theoretically, the vertical resolution of the RO method depends on the gradient of the bending angle with height, and thus

60   the gradient of refractivity with height, and is estimated to be as fine as 100–200 m based on the diameter of the first Fresnel zone at L-band frequencies (Kursinski et al., 1997). However, the measurements at individual tangent point heights are not independent because the ray path samples all atmospheric layers above the tangent point, so the actual resolution is lower. Previous studies have estimated that the typical vertical resolution varies from 100 m near the surface to 1 km at the tropopause (Zeng et al., 2012).

65   Multiple spaceborne missions have deployed GPS receivers on LEO satellites to perform RO observations. The combination of these missions provides a large number of profiles of neutral atmospheric refractivity, temperature, moisture, and ionospheric electron density. Moreover, multiple GNSS constellations are now operational, including GPS, GLONASS, Galileo, and Beidou, which provide more opportunities for RO observations. The Tri-GNSS (TRIG) receiver on COSMIC-2 (Schreiner et al., 2020) now can provide profiles from GLONASS as well as GPS, and Galileo profiles have been demonstrated from aircraft

70   (Haase et al., 2021). The global coverage and high vertical resolution of the spaceborne RO datasets have provided the opportunity to quantify the global properties of gravity waves and other wave sources of variability in the stratosphere. Reviews of the success of RO in capturing equatorial waves are provided in Ho et al. (2019) and Scherllin-Pirscher et al. (2021) and references therein. Several of these studies retrieved information on individual wave events, but were limited to waves with very large horizontal scales and typically greater than 4 km vertical wavelength because the spacing between profiles is irregular and

75   quasi-random in time and space. There is a continuing need to increase the vertical resolution to gain a complete view of the fine-scale wave-mean flow interaction that is unresolved in global models. For example, the difference in momentum between a wave with 4 km vertical wavelength and a wave with 1 km vertical wavelength that dissipates higher in the stratosphere would imply a 40 % difference in the force on the QBO flow.

   The need for a coherent sampling of wave structures in time and space with higher vertical resolution motivates the imple-

80   mentation of the balloon-borne RO observations. The technique has the added advantage of sampling the atmosphere in three dimensions, i.e., to both sides of the flight path along the line of sight to setting and rising GNSS satellites (Haase et al., 2021). Because the balloon carrying the receiver moves at significantly slower speeds than the GNSS satellite, the location of the tangent point (point on a signal ray path closest to the Earth) drifts horizontally from the balloon position at flight level to as much as 500 km from the flight path as the tangent point descends to a height of 4 km. The resulting slanted profile measurements

85   provide an advantage in 3D sampling at the expense of added complexity in interpreting the profiles because of the potential distortion of retrieved wave parameters, such as wavelength and momentum flux (de la Torre et al., 2018). The slanted nature of the profiles also presents difficulties in resolving wave properties in the presence of short horizontal scale variability. The distortion is minimal for larger-scale tropical waves, which are the subject of this study.

   This study is organized as follows: Section 2 briefly describes the methodology of balloon-borne RO. Section 3 gives an

90   overview of the superpressure balloon flights in the Strateole-2 campaign and the balloon-borne RO instrumentation. Section 4 introduces the data analysis procedures and estimates the vertical resolution of balloon-borne RO. Section 5 presents

comparisons of the profiles with other independent datasets from radiosondes and spaceborne RO, as well as comparisons with numerical model reanalyses. Section 6 presents the results illustrating the equatorial waves that are captured with different periods and scales. Section 7 discusses some future perspectives and limitations of the balloon-borne RO observations.

95 Conclusions summarizing the results are presented in Section 8.

2 Method

The GNSS RO technique is a powerful remote sensing technique that utilizes GNSS signals that are refracted and delayed as they traverse the atmosphere nearly horizontally. Vertical variations in atmospheric refractivity and other properties are derived from the signal propagation delays. As a GNSS satellite sets (or rises) relative to a receiver on an airborne or spaceborne

100 platform, the navigation signal scans through the highest to lowest atmospheric layers (or vice versa), which yields a complete profile. In the following, we refer to airborne RO and balloon-borne RO as ARO and BRO, respectively, when necessary to distinguish them from spaceborne RO, which we will refer to as SRO. Unlike SRO, slower platforms flying inside the atmosphere such as aircraft (Haase et al., 2014, 2021) and balloons (Haase et al., 2012) provide a unique opportunity to perform RO measurements continuously in time and space over a localized area, rather than the pseudo-random distribution

105 of the global SRO datasets. The density and continuity are advantageous for reconnaissance flights in an area of interest, such as hurricanes (Murphy et al., 2015; Chen et al., 2018) and atmospheric rivers (Ralph et al., 2020), but can also be applied to the problem of resolving fine-scale wave structures from free-floating balloons. The physics and geometry of ARO and BRO are similar to SRO, but there there are some geometric modifications required to implement the typical RO retrieval technique. The detailed descriptions of the geometry and theory of BRO are provided in appendix A.

110 The atmospheric refractivity N for radio waves at GNSS frequencies (L band) in the neutral atmosphere is described by (Rüeger, 2002)

$$N = (n-1) \times 10^6 = 77.6 \frac{p}{T} - 6.3938 \frac{p_w}{T} + 3.75463 \times 10^5 \frac{p_w}{T^2}, \tag{1}$$

where n is the refractive index, p, p_w and T are atmospheric pressure [in hPa], water vapor pressure [in hPa] and temperature [in K], respectively. In the atmosphere higher than $\sim$10 km, assuming water vapor is negligible, the equation for refractivity can be simplified to

$$N = (n-1) \times 10^6 = 77.6 \frac{p}{T_d}, \tag{2}$$

115 where T_d is commonly referred as dry temperature and deviates from true temperature if moisture is present.

The atmosphere is generally in hydrostatic equilibrium, where the pressure gradient force balances with gravity if there is no acceleration in the vertical direction. It is described by the following equation

$$\frac{\partial p}{\partial z} = -\rho g, \tag{3}$$

where ρ is the atmospheric density. When the atmosphere is perturbed by waves, this equilibrium is no longer satisfied. This is true for high-frequency gravity waves with shorter horizontal wavelengths, and the vertical accelerations cannot be neglected

in the vertical motion of perturbation. However, lower-frequency gravity waves with longer horizontal wavelengths, such as inertia gravity waves, have small vertical accelerations and are consistent with the quasi-hydrostatic approximation.

In this study, dry temperature and pressure were retrieved based on the simplified refractivity formula (Eq. (2)), hydrostatic equilibrium (Eq. (3)), and the ideal gas law $p = \rho R T$, and R is the ideal gas constant. The dry temperature is derived from the following integral,

$$T_d(h) = T(h_0)\frac{N(h_0)}{N(h)} + \frac{1}{R}\int_{z=h}^{z=h_0} g(z)\frac{N(z)}{N(h)}dz. \qquad (4)$$

where $g(z)$ is gravitational acceleration as a function of height, $\frac{N(z)}{N(h)}$ is the ratio of refractivity of two different altitudes. $N(h_0)$ and $T(h_0)$ are refractivity and temperature at the balloon flight altitude h_0, respectively, calculated from in situ measurements.

3 Strateole-2 Campaign

Strateole-2 (STR-2) is an international multi-year series of campaigns that utilize long-duration stratospheric superpressure balloons (SPBs) to investigate the atmospheric dynamics and composition of the tropical tropopause layer (TTL) (Haase et al., 2018). The SPBs fly for several months along the equatorial belt at altitudes of 18–20 km. They are advected by the wind on constant density surfaces, and therefore behave as quasi-Lagrangian tracers in the atmosphere. The first preparatory campaign began in November 2019 with the practical objective of testing the unique capabilities of each of the instrument configurations in advance of the full scientific deployments. Five different instrument configurations were tested on the balloons, some provided in-situ information on the physics, dynamics, particle counts, and greenhouse gas composition of the sampled air parcels surrounding the balloons. Other instruments, including the RO receiver described here, also sampled the atmospheric profiles below the balloons. The preparatory campaign provided initial observations to assess the capabilities of the flotilla to reveal the nature of equatorial waves.
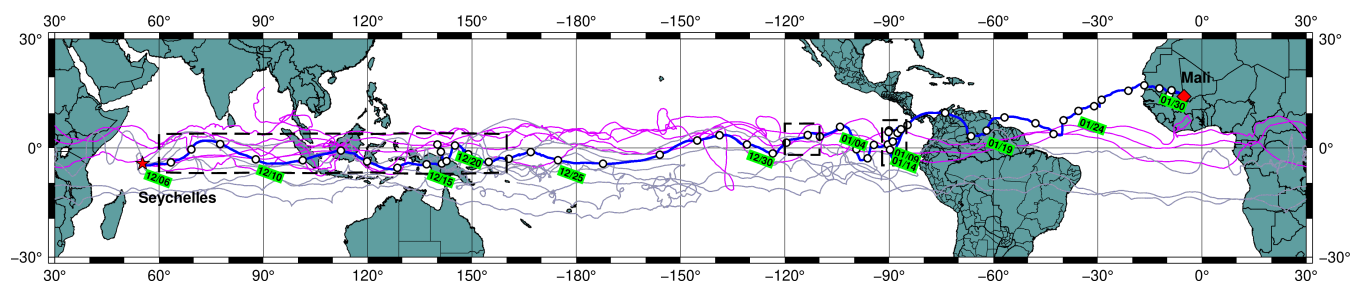
Figure 1. Trajectories of all balloons launched in the Strateole-2 2019 campaign. The thick blue line is balloon "ST2_C0_06_STR1" that carried the radio occultation receiver. ⋆ marks the launch site in Seychelles and ⋄ indicates the final landing site in Mali. Small circles over the trajectory indicate 00Z each day and are labeled at 5 day intervals. Dashed boxes along the trajectory mark the periods when BRO data were recovered. Gray lines are the 4 other balloons flying at ∼20 km, and magenta lines are the 3 balloons flying at ∼18 km.

3.1 Superpressure balloon flights

140 Eight SPBs were launched from Mahé, Seychelles ($4.7°$ S, $55.5°$ E) in the west Indian Ocean over the period from November to December 2019, and flew until late February 2020, achieving a mean flight duration in the tropics of nearly 3 months (85 days). The flight tracks of these balloons are shown in Figure 1. Several balloons completed more than one full circumnavigation at the equator. The 13 meter diameter balloon (labeled as "ST2_C0_06_STR1") that carried the balloon-borne RO instrument was launched on 5 December 2019 and flew eastward at about 20 km altitude for 57 days. Due to a small helium leak in the

145 balloon, it was terminated for safety reasons over the desert in Mali, Africa, on 2 February 2020. The data was transmitted during flight, and the instrumentation was not recovered.

The balloon carrying ROC also carried the Balloon-borne Cirrus and convective overshOOt Lidar (BeCOOL) system to measure optical properties of cirrus in the nadir viewing mode and the topography of convective cloud tops (Ravetta et al., 2020), and the BOLometer Determining Albedo and InfraRed flux (BOLDAIR) to measure upward longwave and shortwave

150 radiative fluxes. The combination of instruments was selected to better understand the modulation of cirrus by wave motions and assess the radiative heating and forcing of the lower stratosphere by water vapor anomalies. The Thermodynamical SENsor (TSEN) meteorological package was included on all balloons to provide in situ measurements which can be used to derive the intrinsic frequency spectrum and probability distribution of gravity waves momentum flux on flight level (Podglajen et al., 2016; Hertzog et al., 2008; Corcos et al., 2021). The balloon-borne RO observations would augment these studies by providing

155 continuous temperature profiles underneath the flight track to resolve the vertical variations. The same instruments flew in late 2021, and will be flown in the forthcoming campaign in late 2024 with 20 balloons, to capture different phases of the QBO.

3.2 Instrumentation

The ROC2 (Radio OCcultation v2) receiver builds on the heritage of the ROC receiver that was originally deployed in the Concoridiasi campaign in Antarctica (Haase et al., 2012; Rabier et al., 2010). It is a low-cost, lightweight multi-GNSS receiver

160 capable of tracking multiple constellations and frequencies with two antennas. It utilizes the sophisticated Septentrio AsteRx-4 OEM board, which performs phase locked loop (PLL) tracking of all GNSS signals in the field of view and is configured to record down to -10° elevation angle below the horizon from the balloon at ~20 km altitude. It also contains a Linux single-board computer (TS-7680) to manage onboard power, configuration, data acquisition, storage, and communication. The superpressure balloons are composed of two gondolas, "Zephyr" for the science payload and "Euros" for flight control.

165 The ROC2 receiver enclosure was installed inside the Zephyr gondola and connected to the two avionics GNSS antennas manufactured by GPSSource, which were installed on the top of the gondola tilted 30 degrees from horizontal in opposite directions. The GNSS antennas were separated as far as possible from the Iridium antenna on the ~50 cm wide gondola to avoid electromagnetic interference because of the proximity of their frequency bands. Also installed in the Zephyr gondola were two other scientific instruments, BOLDAIR and BeCOOL, and the Zephyr On-Board Computer (OBC), which managed

170 the solar-powered battery charging system and the data/command telemetry through the Iridium satellite link. The data were recovered at the Zephyr Mission Control Centre (CCMZ) managed by the Laboratoire de Météorologie Dynamique (LMD) of

the Centre Nationale de la Recherche Scientifique (CNRS) in France. The TSEN package included an Ublox single-frequency GPS receiver on the gondola to provide timing and wind velocity through the real-time positioning solutions. The TSEN thermistor and thermocouple were suspended 8 meters below the Zephyr gondola to provide in situ measurements of ambient temperature at 30 sec sampling interval, and the TSEN barometer was located above in the Euros gondola providing pressure at the same data rate.

3.3 Dataset

The ROC2 receiver continuously tracked multiple constellations including GPS, Galileo, and GLONASS and logged carrier phase, pseudorange and signal to noise ratio (SNR) at a 5 sec sampling interval throughout the whole flight. The logged data was stored in the internal storage of the ROC2 receiver and was transmitted by Iridium data link to the CCMZ every hour. Due to a technical problem that limited the bandwidth of the satellite data link, data from only 23 days of the 57 day flight were recovered. The recovered dataset includes GPS only data from 6 December 2019–22 December 2019, 1 January 2020, 9 January 2021, and 11 January 2021–14 January 2021. The data from three constellations (GPS, GLONASS, Galileo) were recovered from 15 December 2019. A 12 hour test was implemented on 14 January 2021 to track GPS and Beidou constellations, and data were successfully recovered. The locations of the balloon during the period where data were recovered data are marked by boxes on the map in Figure 1.

4 Data Analysis

4.1 Retrieval Procedures

The precise 3-D positions of the balloon were calculated from the GPS pseudorange and carrier phase data using Precise Point Positioning with Ambiguity Resolution (PPPAR) (Ge et al., 2008; Geng et al., 2019) using the Position And Navigation Data Analyst (PANDA) software package developed at Wuhan University (Shi et al., 2008). The procedure was carried out in three steps. The first step was to estimate high rate (30 sec) satellite clock errors based on regional data, instead of using global satellite clock products, since the estimated regional clock solutions can compensate for other unmodeled errors in the PPPAR solution (Lou et al., 2014). GPS satellite orbits were fixed to Center for Orbit Determination in Europe (CODE) final orbits (Dach et al., 2020). Ground GPS observations were used from a list of 26 stations from the International GNSS Service (IGS) network in the equatorial region around the balloon trajectory to solve for the clock parameters (see Figure D1 in Appendix D).

In the next step, fractional cycle biases (FCB) were estimated from the same dataset to improve the resolution of the carrier phase ambiguities (Geng et al., 2011). The final calculation was solved for the coordinates of the balloon antenna at each epoch. The receiver clock errors were also estimated at each epoch as parameters with white noise variance. The zenith hydrostatic delay is constrained to the Saastamoinen model (Saastamoinen, 1972) and the zenith wet delay is assumed to be negligible at the balloon flight altitude and thus not included in the procedures, which reduces the number of estimated parameters. The

estimated position accuracy is $\sim$10 cm in the horizontal, $\sim$20 cm in the vertical and 0.05 m s^{-1} in velocity. The precise position calculation was shown to be a significant improvement over the onboard real-time GPS solution. It has been used to improve the calculation of gravity wave momentum flux from balloon motion variations that treat the balloon as a quasi-Lagrangian tracer (Zhang et al., 2016).

After the precise 3-D positions were determined, they were fixed in the positioning software to calculate the residual distance (excess phase) between the geometric balloon-to-satellite distance and the observed carrier phase using the same satellite clock corrections and models for relativity, antenna phase center corrections, and other effects that were used in the position calculation. The ionospheric effects were corrected using the ionosphere-free combination of dual-frequency (L1 and L2) observations. The excess Doppler for each satellite was calculated by differentiating the excess phase with respect to time. The receiver clock errors were removed by single differencing, where the excess Doppler time series from a high elevation satellite in view at the same time was subtracted from the occulting satellite time series. A second-order Savitzky-Golay filter was used to smooth high-frequency noise in the excess Doppler that would lead to unrealistic variability of shorter scale than the first Fresnel zone. The filtering window width was selected to be 55 seconds based on the vertical resolution analysis in the later sections.

The local radius of curvature, R_c, tangent to the ellipsoidal Earth surface was determined at the approximate location of the lowest tangent point with an orientation parallel to the occultation plane (Syndergaard, 1998). The Cartesian coordinates of the satellite and balloon at each epoch were offset to the new reference frame with origin at the center of curvature. The refractivity at the balloon flight level, $N(h_0)$, was calculated from the in situ pressure and temperature based on Eq. (2) and averaged over the occultation duration to reduce sensitivity to small variations in flight altitude over the duration of the occultation.

The excess Doppler shift was projected onto the satellite-receiver velocities in the shifted coordinate system to calculate the bending angle as a function of impact parameter $a = n(r)r$ as described in Appendix A. Balloon positions and velocities were smoothed using the same filter as the excess Doppler. The refractive index at the balloon location was $n_R = 1 + N(h_o) \times 10^{-6}$. The bending angle was then interpolated to an even sampling of 10 m in the impact parameter. Bending angle was calculated from the satellite observations from 10° above the local horizontal until the signal was lost, so included both positive and negative elevation angle data (see Figure A1). The partial bending angle, α', at each impact parameter, a, below the flight level of the balloon was calculated by subtracting the positive elevation angle observations from the negative elevation angle observations for the same impact parameter (Healy et al., 2002). Finally, a was converted to height above the ellipsoid using $a = n(r)r$ and $h_{\text{ellipsoid}} = r - R_c$. The ellipsoidal height was then converted to the Mean Sea Level (MSL) height by subtracting the geoid height ($h_{\text{msl}} = h_{\text{ellipsoid}} - h_{\text{geoid}}$) retrieved from the EGM96 geoid model at the location of the lowest tangent point. The EGM96 model has a stated accuracy of $\sim$10 cm and horizontal resolution of 15′ (Lemoine et al., 1998).

In practice, even after filtering, the noise in the balloon velocity estimate creates noise in the excess Doppler for positive elevation angles that is comparable to the magnitude of the accumulated excess Doppler due to the atmosphere, so the derived bending angle can be very noisy. In order to reduce this noise, the bending angle as a function of time was heavily smoothed with a loess filter (locally weighted quadratic regression fit) over a 5 min moving window from t_{h_0-1km} to t_{elmax}, corresponding to the time when the tangent point was 1 km below flight level to the time of maximum positive elevation angle.

The bending angle was lightly smoothed with a 1.25 min window for the remaining period for the negative elevation angle. A taper function was used to merge the two bending angle time series between $t_{h_0-0.5km}$ and t_{h_0-1km}. Then we calculated the
240   partial bending angle, which was then much less noisy for all tangent point heights, and computed the refractive index using the inverse Abel transform (Eq. (A3)), with the refractive index n_R at the balloon height fixed. This final estimate of the refractive index should be considered strongly constrained by the in situ refractive index for the top 0.5 to 1 km (Murphy, 2015). These improvements to the bending angle, partial bending angle, and refractivity calculations produce less bias compared to the previous versions of the ARO inversion software developed by Xie et al. (2008) and Murphy et al. (2015), which has been
245   used in multiple aircraft campaigns (Haase et al., 2014, 2021).

    The 1D-VAR algorithm based on the Bayesian optimal estimation theory by combining RO observations and a priori information from a model can be implemented to retrieve a complete set of meteorological parameters, including water vapor pressure (Poli et al., 2002). However, we chose to use dry temperature to avoid any dependence of the retrieval on a first guess model that did not contain any wave signature since the region of interest is above 10 km and BRO is not accurate enough to
250   be sensitive to low values water vapor at those altitudes. This also makes it possible to compare BRO dry temperature profiles directly to SRO dry temperature profiles. The dry temperature profiles were calculated from refractivity and in situ pressure and temperature using Eq. (4).

    Because the motion of the GNSS satellite is much greater than that of the balloon during an occultation, the tangent points drift horizontally away from the balloon as the ray paths vertically scan the atmosphere (Figure A1). For SRO, where the
255   receiver is in a vacuum and the occultation geometry is symmetric within the atmosphere, the horizontal location of the tangent points of each ray path can be solved geometrically. However, this is not the case for BRO, where the receiver is within the atmosphere. The horizontal location at a given tangent point height is determined by a simulation using forward ray-tracing implemented in the Radio Occultation Simulator for Atmospheric Profiling (ROSAP) model (Hoeg et al., 1996; Syndergaard, 1998), assuming a climatological refractivity profile from the CIRA-Q model appropriate for the month and
260   latitude (Kirchengast et al., 1999). The final BRO slant profile dataset includes a horizontal location (latitude/longitude) for each tangent point height in the profile, and the location and time of the lowest tangent point of the profile are provided as the reference for the profile.

    Figure 2 shows the intermediate products of excess Doppler and bending angle for a rising occultation labeled as "G29r_G13". This occultation lasted about 15 minutes from when the receiver started tracking satellite PRN29 and until it rose above the
265   local horizontal. The undifferenced excess Doppler of the pair of satellites is shown in Figure 2(a), and both contain noise on the order of magnitude of $0.05 \, \mathrm{m\,s^{-1}}$. The excess Doppler from the high elevation GPS satellite PRN13 was subtracted from the excess Doppler of occulting satellite PRN29 to eliminate the undetermined receiver clock error. The difference in excess Doppler is shown in Figure 2(b) with interpolation and filtering applied. In this rising occultation, the excess Doppler reached a maximum of $0.9 \, \mathrm{m\,s^{-1}}$. The ratio of carrier to noise density, C/N_o, which indicates the signal power of the tracked
270   satellite relative to the noise floor, fluctuated in the range of 25–45 dBHz when the GPS satellite was deep below the horizon. The C/N_o underwent slight drops around 23.4 h due to the automatic gain control (AGC) in the receiver when signal strength increased, for example, when the satellite rose above the local horizontal. In Figure 2(c), bending angle increases to $0.05°$ as
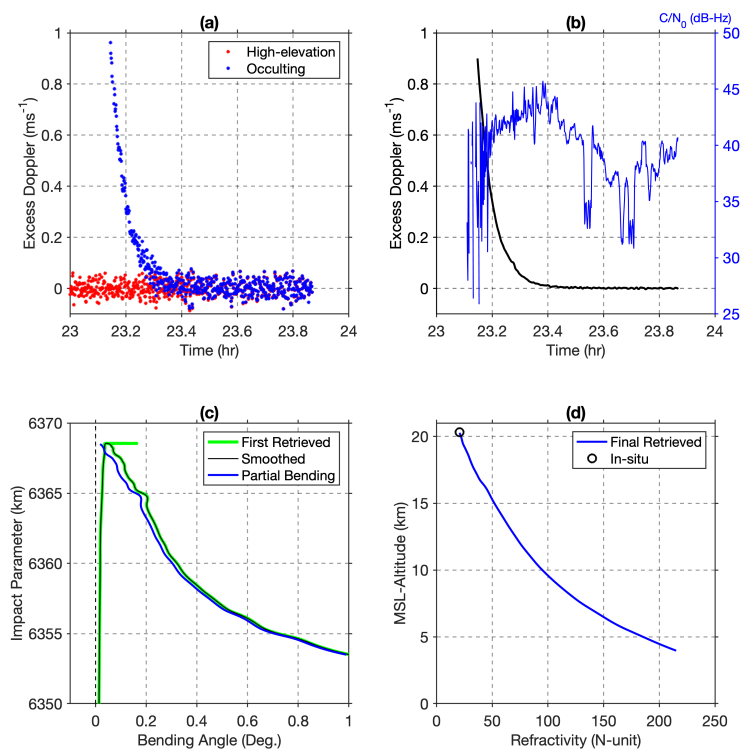
Figure 2. (a) Excess Doppler for the pair of satellites from the rising occultation "G29r_G13". The GPS satellite PRN29 is in the occultation position, and satellite PRN13 at a high elevation angle is used to remove the receiver clock error. (b) The excess Doppler difference for G29 minus G13, after interpolation and filtering (left axis), and signal carrier to noise ratio (C/N_0) (right axis). (c) Bending angle from the initial retrieval (light green) and final retrieval (black) with tapered increased smoothing for the top and positive elevation angle segments of the bending angle (see text). The partial bending angle (blue) is derived from the black curve. (d) The final retrieved refractivity profile with refractivity at the top fixed to the balloon in situ measurement.

impact parameter increases, corresponding to positive elevation angles when the GPS satellite is above the local horizontal, then transitions to decreasing impact parameter as the bending angle increases from $0.1°$ to $1°$ for negative elevation angles

275 when the GPS satellite is below the local horizontal. The green curve shows the raw bending angle without smoothing for the entire occultation, and the black curve shows the bending angle that is smoothed separately and combined with a taper, to reduce the errors propagating into the partial bending. The partial bending angle (blue curve) is obtained by subtracting the positive bending from negative bending at the same impact parameter. The final retrieved refractivity profile is shown in Figure 2(d) in MSL altitude. The resulting refractivity profile from this rising occultation is truncated at 4 km, at the tangent point

280 altitude where the receiver initiated the steady tracking of the GPS signal. A setting occultation would be truncated at altitudes where the receiver loses the tracking of the GPS signal.

4.2 Vertical Resolution of BRO

The GNSS carrier phase data were sampled at a 5 s interval, which would lead to a small vertical sample interval for the tangent points between adjacent ray paths. However, the resolution of RO profiles is determined by the diffraction limit of the signal
285   ray paths, which is defined as the diameter of the first Fresnel zone $Z_F = 2\sqrt{\frac{\lambda L_T L_R}{L_T + L_R}}$ where λ is the GPS signal wavelength (0.19 m for GPS L1), and L_R and L_T are the distances from the receiver and transmitter to the tangent point of the ray path (Hajj et al., 2002; Kursinski et al., 1997). For a stratospheric balloon flying at 20 km altitude, L_R is a maximum of 600 km, and L_T is about 25,800 km for GPS satellites, which yields a maximum of $Z_F \sim 600$ m. It is smaller than SRO, where Z_F is about 1.4 km because the LEO satellites are at higher altitudes and thus further away from the tangent point of the ray
290   path. When the vertical gradient of refractivity is considered, the vertical resolution can be described as $Z_F^\star = Z_F \sqrt{M}$, where the defocussing factor M is defined as $\left(1 - \frac{L_T L_R}{L_T + L_R}\frac{d\alpha}{da}\right)^{-1}$. The diffraction-limited vertical resolution of the BRO profiles in a realistic atmosphere lies in the range 200–500 m. As shown in Figure 3(a), the vertical resolution is higher at the highest altitude near the tropopause because the tangent point is closer to the balloon and in the lowest 4 km because of the increasing refractivity gradient. In the retrieval procedure described in section 4.1, the time scale of the Doppler smoothing is consistent
295   with this vertical resolution, i.e., the time for the tangent point to cross the first Fresnel zone diameter $T = \frac{Z_F}{V\sqrt{M}}$ where V is the vertical velocity of the ray path tangent point in a vacuum. In Figure 3(b), the vertical velocities of the tangent points in the atmosphere were shown to vary among different BRO profiles over one day (12 December 2019) due to slightly different occultation geometries. The estimated time for the ray tangent point to cross the diameter of the first Fresnel zone is around 20–60 sec above 5 km, and around 100–800 sec below 5 km. The time window selected for excess Doppler filtering is 55 sec
300   (11 data points), which is intended to filter out the majority of variations of the sub Fresnel zone scale for data above 5 km. Evidence for the fact that BRO has a higher vertical resolution (smaller Z_f) than SRO is exhibited in Figure 6 where the cold point tropopause (CPT) layer appears thinner in the radiosonde and BRO profiles than in the COSMIC-2 profile, and in Figure 9 where additional variability is indicated in the BRO–COSMIC-2 comparison at $\sim$18 km altitude.

5   Retrieval Results and Data Quality

305   During the first 17 days of the flight (06 December 2019–22 December 2019) when a nearly continuous sequence of data was recovered, there are about 750 BRO profiles retrieved from the GPS satellites alone (top panel of Figure 4). On average, there are 44 profiles retrieved per day. The sampling of the profiles is consecutive in both time and space, in contrast to SRO that has an almost random distribution. The balloon was drifting predominantly eastward with an average velocity of 10–15 m s^{-1}, at a time when the QBO was in the westerly phase of zonal mean winds. The profiles were distributed in a band within $\pm 10°$ of the
310   equator with an average separation of $\sim$100 km. The density of profiles over a given area varies with wind speed. The balloon path shows meridional motions associated with wave periods of $\sim$3–4 days. From 16–19 December 2019, the zonal wind was relatively weak, producing a very dense sampling of BRO profiles near 140° E longitude. The sampling was similarly dense between 9 and 14 Jan 2020 near -90° E longitude.
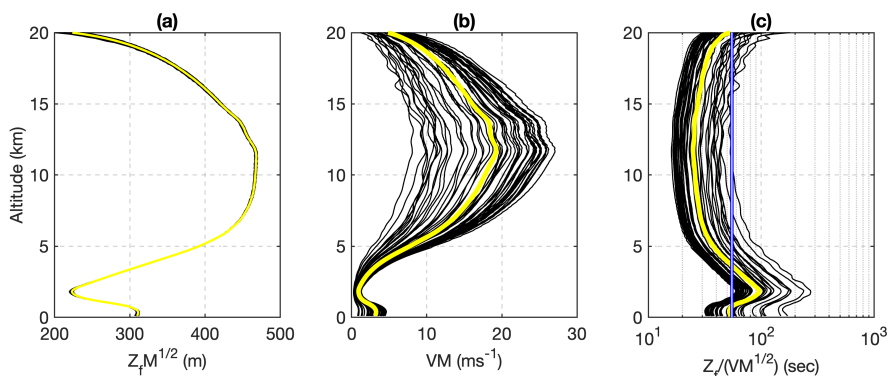
Figure 3. (a) Diameter of the first Fresnel zone of the radio wave for BRO profiles from 12 December 2019. Thin black lines are individual BRO profiles, and the thick yellow curve is the daily mean for all panels. (b) Vertical velocity of the ray path tangent point during the occultation. (c) Time for the tangent point to cross the first Fresnel zone diameter as a function of height. The thin blue line indicates the selected window width used to filter the excess Doppler.
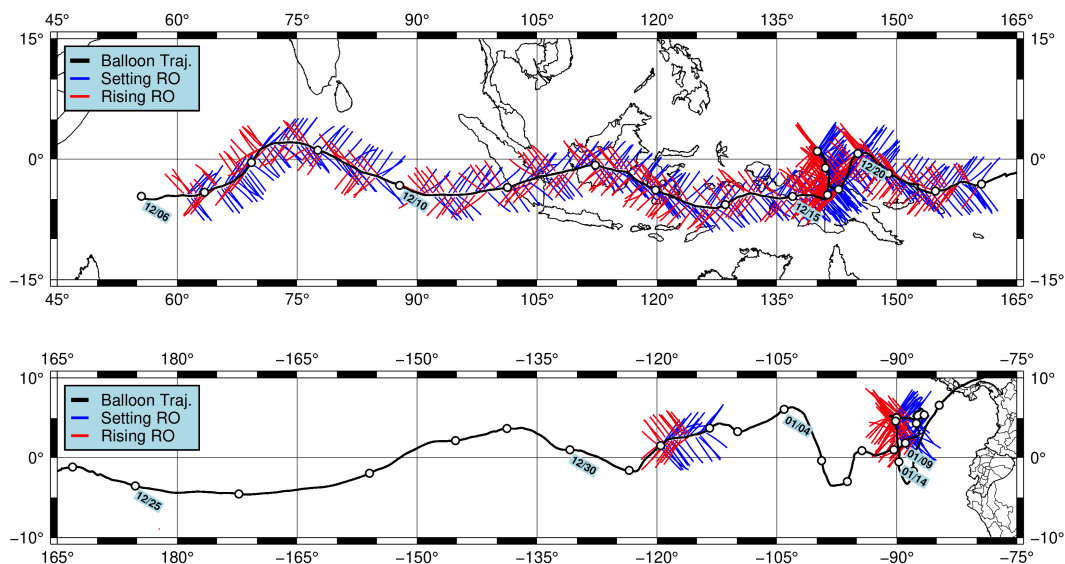
Figure 4. Plan view of the slant BRO profiles from 06 to 22 December 2019 (top), and a few selected days in January 2020 (1, 9, 11, 12, 13) (bottom). The thick black line marks the trajectory of the balloon at the altitude of ∼20 km. Red and blue lines denote rising and setting BRO profiles, respectively, with the lowest tangent point the furthest from the balloon path. Small circles mark 00Z each day and are labeled with the date at 5 day intervals. Galileo and GLONASS data were recovered on 15 December and Beidou data were recovered on 14 January but not included in this map.

GPS satellites travel much faster (2,000 m s^{-1}) at much higher orbits (20,200 km) than superpressure balloons drifting with
the wind at 20 km altitude. Over the duration of an occultation lasting about 10–20 minutes, the balloon is relatively stationary
compared to the GPS satellite. For a setting occultation, the tangent points of the ray path descend and drift horizontally away
from the balloon position as the satellite sets (blue lines in Figure 4), and vice-versa for rising occultations (red lines in Figure
4). The slant profiles are aligned in four primary directions, roughly parallel to the orbital planes of the GPS satellites at the
equator (55° orbit inclination). Rising occultations on the north side of the balloon sample roughly from NW to SE and on
the south side sample from SW to NE. Setting occultations sample from SW to NE on the north side of the balloon and NW
to SE on the south side of the balloon. The temporal sampling of tangent points in an individual profile always produces later
sampling to the east. Within a short time window, four or more setting and rising profiles form a tetrahedral shape extending
500 km in 4 different directions. This nearly orthogonal distribution of BRO profiles is expected to present advantages for
resolving wave structure in the horizontal direction. Multiple consecutive profiles form a train of near-parallel transects ∼400
km wide along the trajectory.
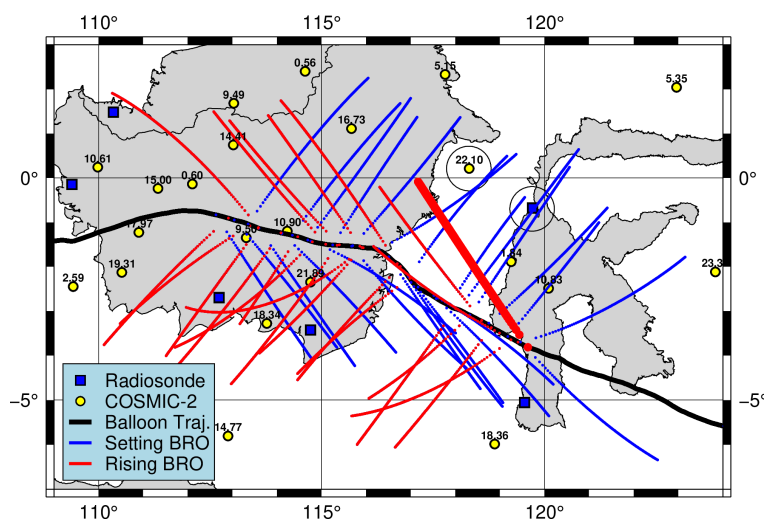
Figure 5. Spatial distribution of the slant BRO profiles on 12 December 2019. The thick black line marks the trajectory of the balloon at
the altitude of ∼20 km. Red and blue lines denote tangent point locations for rising and setting BRO profiles, respectively. Blue squares
denote radiosonde stations, and yellow circles denote COSMIC-2 RO profiles over the same day (without considering horizontal drift). The
numbers above the yellow circles are the time in hours of the COSMIC-2 RO profiles. The BRO profile denoted by a thick red line and the
circled COSMIC-2 and radiosonde profiles are close in space and time, thus selected for comparison in Figure 6. The transect of setting
(blue) BRO profiles on the south side of the balloon trajectory is shown in Figure 7. No COSMIC-2 RO profiles are obscured by the legend
in the lower-left corner.

The spatial distribution of the 49 BRO profiles retrieved from GPS satellites on 12 December 2019 is shown in Figure 5.
There are 23 rising occultations (red) and 26 setting occultations (blue). The thick black line is the balloon flight track, and the
balloon was flying eastward over Indonesia during that period. The profiles are relatively evenly distributed and continuous in

both time and space, which provides a comprehensive sampling of the atmosphere beneath and surrounding the flight track. A

330   typical BRO tangent point profile will drift as far as 500 km to the side of the flight path as the tangent point altitude decreases
from balloon flight level down to 4–5 km altitude, producing the sequence of points appearing as curved lines in Figure 5.
The horizontal drift is greater at the top and varies slightly depending on the relative orientation of the satellite motion to the
occultation plane. The horizontal drift is much larger than SRO over the same altitude range. For most of the occultations (41
out of 49), the lowest tangent point altitude reaches below 10 km, and the deepest profile reaches 4 km. About 22 SRO profiles

335   from COSMIC-2 fell in the map area on that day. However, they are scattered randomly in both space and time, as shown in
Figure 5.

To evaluate the quality of the BRO observations, we compared them with observations from radiosonde launches when
the balloon passed over the maritime continent. We also compared them with COSMIC-2 SRO profiles that were close in
location and time and with reanalysis products from the European Centre for Medium-range Weather Forecasting (ECMWF)

340   Reanalysis-5 (ERA5) (Hersbach et al., 2020). The hourly ERA5 reanalysis (European Centre for Medium-Range Weather
Forecasts, 2019) interpolated from native model levels was chosen to represent the best estimate of the atmosphere state
for this study, particularly for its high vertical resolution in the UTLS (∼300–400 m) and high temporal resolution of one
hour. These ERA5 model level products have a horizontal resolution of $0.25° \times 0.25°$ (∼25–30 km) and 137 hybrid sigma-
pressure levels in the vertical, up to a top-level of 0.01 hPa. The geopotential and geometric height, and the pressure at each

345   of the aforementioned model levels, were calculated using the method employed at the ECMWF (Simmons and Burridge,
1981; Trenberth et al., 1993). For each retrieved BRO profile, a corresponding refractivity profile from the ERA5 product was
created by extracting the horizontal grid point closest to the observed tangent point for the nearest hour. Linear interpolation
for temperature, specific humidity, and the logarithm of pressure was performed between the two nearest model levels in the
reanalysis product to the height of the given tangent point in the BRO profile. Therefore, the final matching reanalysis profile

350   also drifts horizontally and contains the same number of points as the given BRO profile. Note that the ERA5 products on
pressure levels do not preserve sufficient vertical resolution to represent fine vertical-scale waves.

Figure 6(a) shows a BRO profile with the radiosonde observation at Mutiara Airport near Palu, Indonesia (station ID# 97092)
and a COSMIC-2 RO profile (locations circled in Fig. 5). They were located about 300 km and 150 km away from the BRO
profile, respectively, and the time differences were less than 2 h. The refractivity profiles were calculated from the dropsonde

355   and ERA5 products using Eq. (1) with water vapor pressure estimated from specific humidity (details in Appendix C). The
matching ERA5 profile at the drifting tangent points is also shown in Figure 6(a). At each hour, we calculate the mean balloon
location, then average all of the COSMIC-2 profiles that occur within ±15 days of that time and ±5° latitude and longitude
of that location to construct a monthly mean background refractivity and temperature profile that captures synoptic-scale
variations at periods much longer than the expected wave signatures. This COSMIC-2 "monthly mean" profile best represents

360   the mean tropopause structure, excluding the influence of tropical waves. In Figure 6(b), the percentage refractivity difference
relative to the monthly mean profile is shown. The observations all show similar deviations from the monthly mean climatology.
The BRO, radiosonde, and COSMIC-2 profiles all contain small-scale wave features near and above the tropopause. The wave

features are also present in ERA5, which assimilates both radiosonde and COSMIC-2 data. Visually, the BRO profile matches the ERA5 profile well for this case, which we attribute to the fact that they both consider the same tangent point drift.
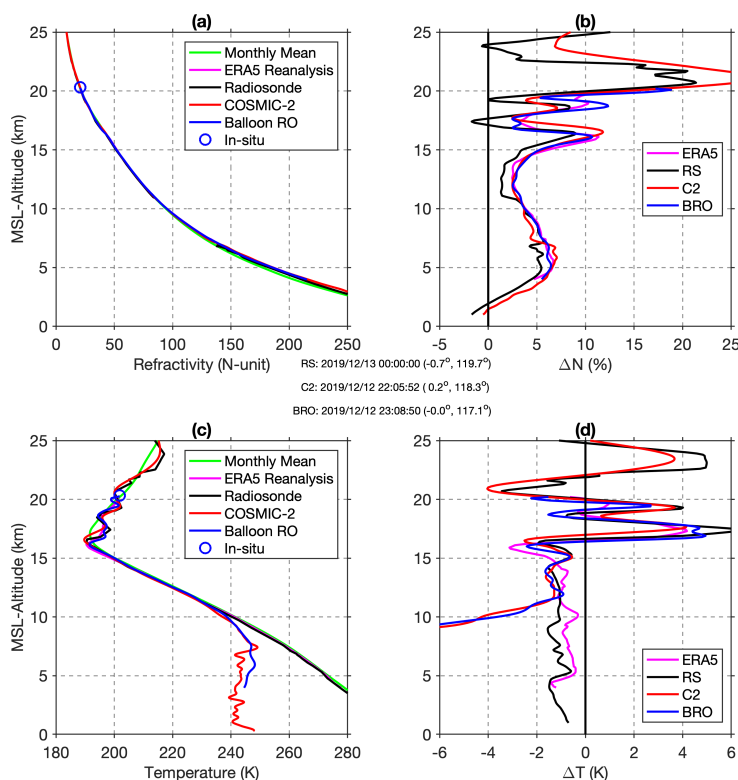
Figure 6. (a) Refractivity profiles from BRO, the ERA5 reanalysis, a nearby radiosonde (RS), a COSMIC-2 RO profile (locations shown in Fig. 5) and the monthly regional mean determined from COSMIC-2. (b) Percentage refractivity differences of ERA5, radiosonde, COSMIC-2, and BRO with respect to the COSMIC-2 monthly mean. (c) Corresponding temperature (dry temperature for COSMIC-2 and BRO) profiles. (d) Corresponding temperature differences with respect to the COSMIC-2 monthly mean. The time and location of the radiosonde, COSMIC-2 RO and BRO are listed in the panel.

365   The refractivity differences between the BRO and the radiosonde is ∼1 % from 4 to 15 km and ∼2 % above 15 km. Note that the radiosonde site is closer to the lower part of the BRO profile, as shown in Figure 5, and the BRO profile is within an hour of the 00:00UT launch time. Considering the spatial and temporal separation between the BRO and radiosonde measurements, the BRO profiles have an absolute accuracy better than 2 %. The temperature profiles (dry temperature for COSMIC-2 and BRO) are shown in Figure 6(c). The BRO dry temperature closely matches the radiosonde and COSMIC-2 temperature above

370   10 km and resolves the cold point tropopause very well. Figures 6(d) shows wave temperature anomalies (absolute differences) from the COSMIC-2 monthly mean profile. A similar wave pattern can be identified in all observations, and waves are seen to sharpen and depress the cold point tropopause by ∼1 K, as has been observed in previous studies (Kim and Alexander, 2015). The differences in temperature between the BRO, COSMIC-2, and radiosonde are within 1 K above 10 km. Below 10 km,
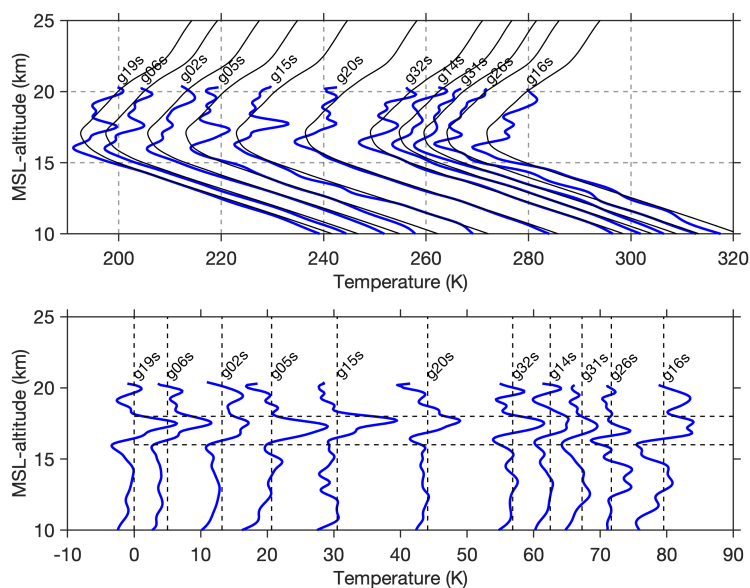
Figure 7. (Top) Transect of northwest-southeast oriented BRO temperature profiles (blue lines) from 12 December 2019 south of the balloon trajectory (see Fig. 5; blue lines) ordered by time and the offsets are proportional to the intervals. COSMIC-2 background profiles are shown as black lines. (bottom) BRO profiles with the background removed. A coherent wave structure with ~4 km wavelength dominates the variability.

the BRO and COSMIC-2 profiles are similar, as they both neglect water vapor and thus are not comparable to ERA5 and the radiosonde.

The wave pattern observed in the radiosonde, COSMIC-2, and BRO profiles in Figure 6 can be examined in more depth, given a large number of BRO profiles available. Figure 7 shows a series of 11 profiles that were collected consecutively in space and time from setting GPS satellites on the south side of the balloon track on the same day (12 December 2019), where the orientations of the tangent point drift were similar. The offsets between two adjacent profiles are proportional to the interval between them. The CPT is at ~16 km and is associated with a vertical wave pattern that is common to all the profiles. This is even more clear when the large-scale background temperature profile is removed, shown in the lower part of Figure 7. The background has its coldest point significantly higher, at ~17.5 km. This fine-vertical scale (~3–4 km) wave pattern seen in the BRO data must have a long intrinsic period (>1 day) since no obvious progression in phase is visible.

A statistical comparison between BRO and the corresponding ERA5 reanalysis profiles for the entire 17 day period is shown in Figure 8. The number of points from the BRO profiles at each height is indicated in black lines. The lowest tangent point altitude in each profile varies because the PLL receiver loses or initiates tracking of different satellites at different altitudes. Most of the profiles (~600) penetrate below 10 km, and ~400 profiles penetrate below 8 km. The differences are characterized by the mean and standard deviation (SD) of the absolute and percentage differences between the two datasets. The mean difference between BRO refractivity and ERA5 is within 0.1 N-units, and the corresponding percentage difference is about 0.2
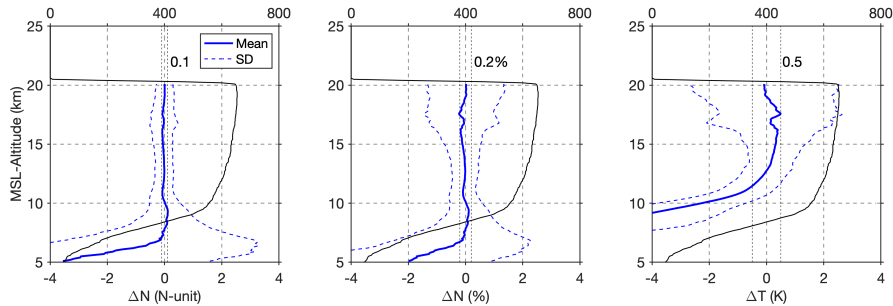
Figure 8. (Left) absolute refractivity difference between BRO and ERA5 (BRO minus ERA5), (center) percentage refractivity difference and (right) absolute temperature difference. Blue solid and dashed lines are the mean and standard derivation (SD) of the differences between the two datasets. Note that true temperature is shown for ERA5 and dry temperature is shown for BRO. The number of BRO measurements at each altitude is shown by the black line and top axis. For reference, the vertical dotted lines around zero represent 0.1 N-unit and 0.2 % in absolute and percentage differences and 0.5 K in temperature difference.
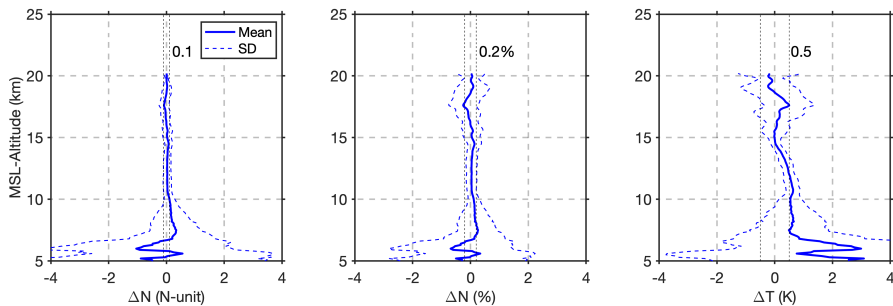
Figure 9. (Left) absolute refractivity difference between daily mean BRO and daily mean COSMIC-2 RO (BRO minus COSMIC-2), (middle) percentage refractivity difference and (right) dry temperature difference. The COSMIC-2 profiles are within 10° latitude and 10° longitude of the daily mean balloon position. Vertical dotted lines around zero represent 0.1 N-unit and 0.2 % in absolute and percentage difference, and 0.5 in dry temperature.

% above 7 km. The mean difference between retrieved dry temperature and ERA5 is within 0.5 K above 11 km, where moisture is negligible, with BRO showing higher temperatures. A residual wave-like pattern is apparent in the differences above 15 km, which is likely the signature of a large-scale and slowly varying wave captured by BRO that is coherent over the 17 days and is not captured accurately or is underrepresented in ERA5, as seen in Figure 6(c) and Figure 7. Because the dataset extends only ~100° longitude along the equator, the large-scale wave perturbations were not averaged out and are still evident in the BRO dataset.

Although there are many COSMIC-2 profiles over the equatorial region during the period of the Strateole-2 campaign, the number of profiles available to implement a profile-to-profile comparison between the two datasets is quite small. In order to compare the two types of RO profiles, the daily mean refractivity and temperature were calculated for each dataset by averaging

all RO profiles that occurred over a day within a box of 10° latitude by 10° longitude centered on the mean balloon position for the day. There were typically about 15–25 COSMIC-2 profiles per day falling in such an area compared to ~45 BRO profiles. There are in total 17 daily mean profiles calculated for both RO datasets. Figure 9 shows the absolute and percentage differences of daily mean refractivity between BRO and COSMIC-2. There is about a 0.1 N-unit mean difference between the two datasets above 15 km, corresponding to a 0.2 % difference. The mean temperature difference is within about 0.5 K between two RO datasets above 8 km, with BRO showing higher temperatures. The largest differences at 17 km altitude close to the tropopause suggest that the COSMIC-2 daily mean may not be capturing all of the wave structure present in the higher vertical resolution BRO observations. Residual wave effects may also be associated with the limited sampling of COSMIC-2, or the latitudinal dependence of waves that may result in averaging out some variability. The technique for constructing composites of COSMIC-2 data is explored further in section 6. Between 7–15 km, the differences are very small and stay within 0.1 % of the refractivity. The BRO observations are expected to be noisier than COSMIC-2 RO near the top of the profile because the accumulated bending angle along the ray path and the excess Doppler is small compared to velocity errors from the position uncertainty (Muradyan et al., 2011). However, the in situ refractivity observations assure the errors are small. The comparison between the two datasets illustrates that the same technique on different platforms can consistently observe large-scale atmospheric properties. The difference seen in the dry temperature below 15 km might be due to the different numerical schemes of calculating the dry temperature in the two datasets.

6 Equatorial Waves in the BRO Dataset

A primary objective of this work is to determine the properties of the equatorial waves that are evident in the BRO dataset, such as presented in Figure 7. The TSEN instrumentation on the Euros gondola measures flight level temperature and horizontal wind from the balloon position and reveals some properties of the wave spectrum. The Lagrangian frame of reference on the drifting balloon enables a direct measurement of intrinsic wave frequencies. From these measurements, we compute the wave energy spectrum as a function of intrinsic frequency over the 57 day flight, which contains the period of high-density BRO measurements. Figure 10 shows the spectrum for waves with periods 1–30 days. The spectrum shows a main peak near 20 days and secondary peaks at 3–4 days plus a background of higher-frequency waves. The 20 day signal is associated with a large quadrature in zonal wind and temperature without any coherent meridional wind signal (not shown), permitting interpretation of the 20 day signal as a Kelvin wave. The clear break in the spectrum near 5 day is next selected as the cutoff period for filtering to separate this Kelvin wave from shorter period waves in BRO temperature profiles.

Given the characteristics of the profile transects shown in Figure 7, we investigated the ability of BRO profiles to capture the properties of equatorial waves with short vertical wavelengths. In order to extract the wave components, background temperature profiles were subtracted from each BRO profile. The background temperature is defined as the moving average of all COSMIC-2 profiles that occurred within ±15 days and ±2° latitude and ±10° longitude surrounding the balloon location. Temperature perturbations thus include waves with periods shorter than 30 days, including Kelvin waves through shorter period gravity waves. The BRO temperature perturbation profiles in Figure 11(a) are ordered in time along the balloon track, with the
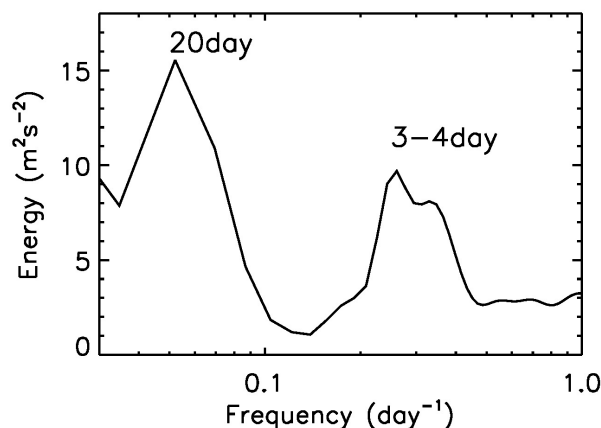
Figure 10. Intrinsic frequency spectrum of total wave energy $(\mathrm{m^2\,s^{-2}})$ from TSEN measurements at the balloon float altitude near 20 km for the flight containing the time of the high-density BRO measurements.

corresponding longitudes shown on the top axis. The altitude of the BRO cold point tropopause (CPT) is also shown in Figure 11(a). The coherent descent of phase with time, characteristic of upward propagating tropical wave energy, is observed in the stratosphere, as well as variability on a wide range of time scales. The longer period coherent wave is clear in the BRO profiles that are filtered within periods of 5–30 days shown in Figure 11(c).

Figure 11(b) shows the residual temperature variation after removing the dominant long period signal from Kelvin waves (5–30 day period) shown in figure 11(c). This isolates the tropical wave variability at periods ≤5 day. These shorter period wave signals commonly reach ±4 K, and coherent phase descent is evident at times. Variability at the shortest time scales may be convolved with spatial wave variability, and multiple waves may be present, so further study of these high frequencies will be the subject of future work. Previous analyses of ground-based tropical observations at fixed locations have chosen a cutoff period at ≤3 day to isolate inertia-gravity waves (Sato and Dunkerton, 1997). Pass bands of ≥4–7 day periods have been used to isolate Kelvin waves (Tsuda et al., 1994; Kiladis et al., 2009). However, these analyses were done in the ground-based reference frame, while we observe in the Lagrangian frame and at latitudes very close to the equator. This frame of reference difference is an important distinction, and we will show clear differences in waves observed in these two frames of reference in what follows. While mixed-Rossby-Gravity waves and Kelvin waves can occur near a 5 day intrinsic period, we do not observe these signals around this period of high-density BRO data.

Figure 11(c) shows the filtered temperature perturbation within the period band of 5–30 days, which contains Kelvin waves with a peak period of ∼20 days in these BRO data. The vertical structure of the 5–30 day signal in Figure 11(c) has a dominant vertical wavelength of ∼6 km until day 350. Then after day 352, a ∼3 km vertical wavelength signal is more prominent. We can estimate the horizontal wavelength using the dispersion relation for Kelvin waves,

$$\hat{\omega} = Nk/m, \tag{5}$$
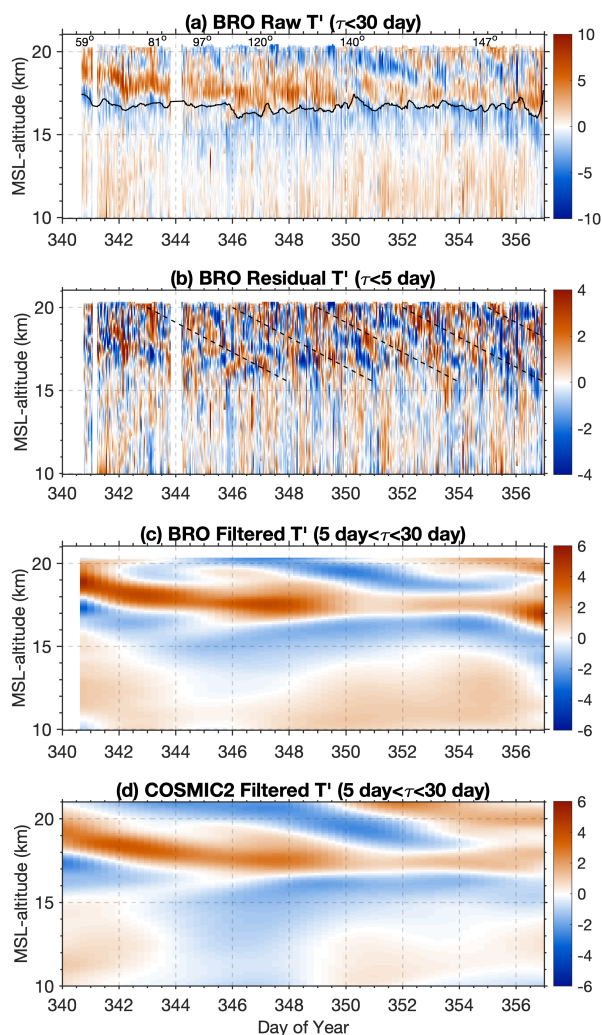
Figure 11. Time-altitude cross-section of the 17 days continuous measurement period. (a) BRO temperature perturbations with periods less than 30 days, (b) BRO temperature perturbations with periods less than 5 days after removal of Kelvin waves, (c) BRO Kelvin wave perturbations (periods in the band 5–30 day), (d) COSMIC-2 Kelvin wave perturbations (5–30 day) from compsite profiles. Black lines in (a) mark the cold-point tropopause height. Numbers at the top axis of (a) are the longitudes at the corresponding time.

where $\hat{\omega}$ is intrinsic frequency, N is buoyancy frequency ($\sim$.025 s^{-1}), and k and m are horizontal and vertical wavenumber, respectively. The 6 km signal is thus associated with the wavenumber (wn) 1 Kelvin wave and the 3 km signal with wn 2.

A comparable estimate of the 5–30 day period Kelvin wave perturbations observed by COSMIC-2 is demonstrated by constructing composite temperature profiles following the balloon trajectory. These profiles were obtained by averaging the
455   COSMIC-2 profiles that occurred within ±12 hours and $\pm2°$ latitude and $\pm10°$ longitude of the hourly mean balloon location. Then, the same previously defined monthly mean background was removed from these profiles. The residual temperature
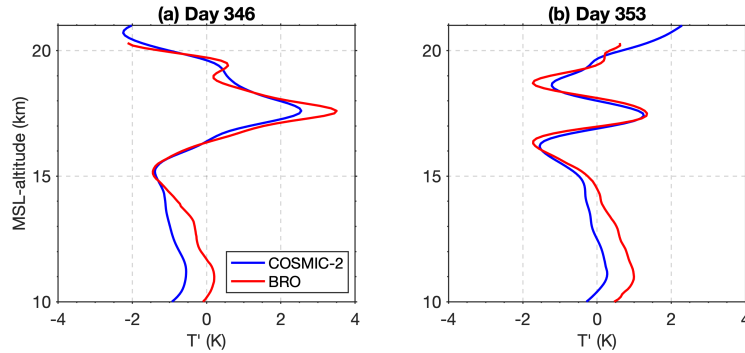
Figure 12. Profiles of Kelvin wave temperature perturbations from COSMIC-2 and BRO from Fig. 11(c) and (d), on (a) day 346 when the 6 km vertical wavelength dominates and (b) day 353 when the 3 km wavelength dominates.

perturbations are shown in Figure 11(d). The pattern is very similar in the BRO and COSMIC-2 observations, but the amplitudes in the BRO appear stronger, particularly in the later period where the 3 km vertical wavelength structure dominates. The larger amplitude of the Kelvin wave signal in the BRO data can be explained by the higher vertical resolution of BRO compared to

460 SRO derived in section 4.2. Figure 12 shows this more quantitatively by comparing profiles in Figure 11(c) and (d) on days 346 (when the 6 km wavelength dominates) and 353 (when the 3 km wavelength dominates). The same Kelvin waves are well observed by both datasets; however, the ones observed by COSMIC-2 show amplitudes attenuated by ∼20 % compared to BRO. The discrepancies below 15 km might be due to different numerical schemes of calculating the dry temperature from refractivity, which can also be seen in Figure 9(c).

465 To illustrate the effect of the balloon's Lagrangian frame of reference on wave observations, Figure 13 shows temperature perturbations in the ground-based frame of reference. In panel (a), the COSMIC-2 data shown is from the daily average of temperature profiles within a fixed area (a box from 120° E–140° E, and 2° S–2° N), band-pass filtered between 5 and 30 days. In panel (b), radiosonde data from Manado, Indonesia, (Station# 97014, 124.91° E, 1.53° N) is high-pass filtered for periods shorter than 5 day. Both datasets are organized by altitude and time for comparison with the BRO dataset, filtered for

470 the same periods. Unlike the BRO dataset in the Lagrangian frame as shown in Figure 11, the filtered COSMIC-2 temperature perturbations within periods of 5–30 day (Kelvin wave signal) show different features. Figure 13(a) shows a relatively steady downward progression of phase in time in this ground-based frame. During days 340–350, the period of the wn=1 Kelvin wave observed in this frame is closer to 16 days, shorter than the 20 day observed in the TSEN data. This intrinsic period could also be resolved by BRO data given that more data was retrieved.

475 Linear wave theory predicts that the difference between ground-based frequency and intrinsic frequency is equal to the zonal mean QBO wind (U) times wavenumber k,

$$\omega_0 - \hat{\omega} = Uk. \tag{6}$$
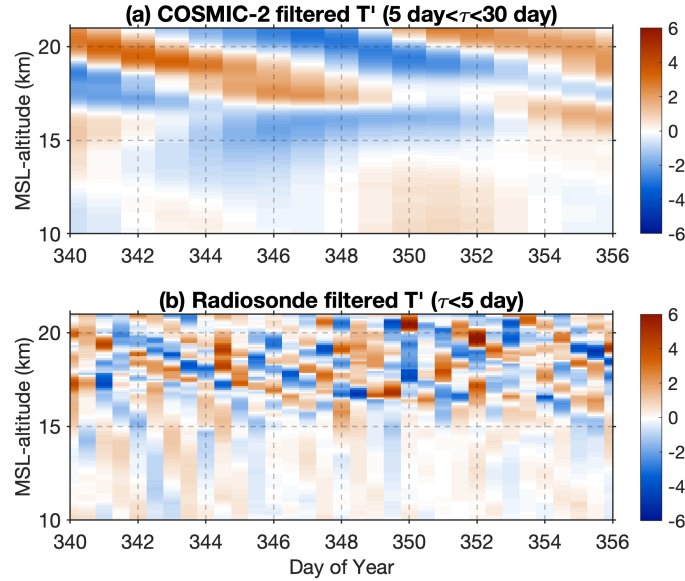
Figure 13. (a) Time-altitude cross-section of COSMIC-2 temperature perturbations binned at a fixed location surrounding the radiosonde site (120° E–140° E, 2° S–2° N) and band-pass filtered at 5–30 day period. Time is indicated with daily values at 12 UT on the horizontal axis. (b) Radiosonde (124.91° E, 1.53° N, station ID# 97014) temperature perturbations high-pass filtered for periods shorter than 5 day. Time is indicated with daily values at 0 UT and 12 UT on the horizontal axis.

The difference is therefore consistent with an eastward mean wind of $U \sim 8 \, \mathrm{m \, s^{-1}}$, a value closely matching the observed zonal wind. Kelvin waves have strong zonal wind perturbations that are in quadrature with the temperature perturbations (Andrews et al., 1987). In the Lagrangian frame, the balloon moves faster during the eastward Kelvin wave phase. During the westward
480 phase of the Kelvin wave, the balloon slows considerably, but during part of that time it is still moving eastward. Thus when the balloon and wave move in the same direction and the wave propagation is faster than the mean wind, the balloon spends more time in eastward motion, and shorter time in westward motion. This difference would be reversed if the QBO were in the westward phase.

As presented in Sato and Dunkerton (1997), the Kelvin wave momentum flux is related to the quadrature spectrum of
485 temperature and zonal wind perturbations.

$$\overline{u'w'} = -\frac{g}{\overline{T} N^2} \int\limits_{\omega_1}^{\omega_2} Q_{Tu}(\hat{\omega}) \, \hat{\omega} \, d\omega, \tag{7}$$

where $Q_{Tu}(\hat{\omega})$ is the quadrature spectra of the temperature and zonal wind fluctuations at intrinsic frequency $\hat{\omega}$, $\overline{T}$ is the background temperature, and N^2 is squared buoyancy frequency. This is a direct estimation of total momentum flux that contains both positive and negative momentum flux. The quadrature spectrum of temperature and zonal wind perturbations were calculated from the TSEN measurements; a peak of about -3 $\mathrm{K \, m \, s^{-1}}$ was found for the 20 day Kelvin wave around

490   the BRO high-density observation period (not shown). Assuming a background temperature of 195 K and a density of $\sim$0.1
kg m^{-3} at about 20 km, the total momentum flux associated with the Kelvin wave is calculated to be around 0.087 mPa. This
is consistent with the results deduced from radiosonde data during the same phase of the QBO, which is about 0.1–0.2 mPa
at around 20 km (Sato and Dunkerton, 1997, Fig. (7)). The slight discrepancy is likely because the ground-based, rather than
intrinsic frequency was used in the calculation, which results in an overestimate of momentum flux.

495   Figure 13(b) shows the high-pass (5 day cut-off period) filtered radiosonde temperature anomalies. Again differences be-
tween perturbations in this ground-based reference frame and in the Lagrangian frame (Figure 11b) are apparent, but with
many different frequencies and wavenumbers of gravity waves likely contributing to these perturbations, the interpretation is
more complex and left to future work.

We note that theoretical dispersion curves for equatorial waves (e.g., Kiladis et al. (2009)) are calculated in the intrinsic
500   (Lagrangian) reference frame, so BRO measurements provide a unique advantage for the interpretation of equatorial waves.
This unique BRO dataset, together with data from other instruments onboard the same balloon and other Strateole-2 balloons,
will provide an opportunity to study the fine vertical structure of waves in the tropical tropopause layer (TTL) and below, and
to investigate their relation to tropical convection and convectively-coupled equatorial waves.

7 Discussion

505 We have shown the level of consistency of the BRO observations with radiosonde observations, and made statistical comparisons with the ERA5 reanalysis and COSMIC-2 RO for the larger horizontal scale Kelvin waves, which provides confidence in the information extracted from the BRO observations. RO has been deployed on many satellite missions to provide increasing global coverage, either as a primary payload in dedicated constellations or as a secondary payload in other science missions, and recently in commercial CubeSat constellations. The BRO observations extend the general capabilities of GNSS RO to

510 dense consecutive profiles that can be exploited to investigate coherent finer vertical scale wave variability, as illustrated above. There is a rich dataset still to be explored in terms of three-dimensional propagation characteristics and directionality by analyzing transects with different orientations from the orthogonal pattern of tangent point profiles. These capabilities will be further enriched by implementing the tracking of multiple constellations, including Galileo, GLONASS, and Beidou. On average, there were $\sim$2 profiles retrieved per hour from the GPS constellation. Including data from multiple GNSS constellations

515 more than doubles the number of profiles, as was seen in the technology evolution for aircraft ARO observations (Haase et al., 2021). The multi-constellation recordings that were successfully tested for one day during this campaign are planned to be implemented for future Strateole-2 science campaigns which will have increased communications bandwidth. Multi-constellation recordings will further improve spatial and temporal resolution.

The BRO observations of temperature variability in a moving reference frame provide a unique benefit when interpreting

520 characteristics from dispersion relations. Strictly speaking, the dispersion relations that relate intrinsic period to wave speed hold in the intrinsic (Lagrangian) reference frame. Infrared satellite data that are often used to capture wave modulation of deep convection (i.e., Kiladis et al. (2009) are typically displayed and analyzed in an Earth-fixed (i.e., ground-based) reference frame. In the troposphere, where the winds are lighter and more random, the approximation that the reference frames are nearly equivalent has a negligible effect. However, in the stratosphere, where the mean flow is stronger, the wave dispersion curve

525 in the intrinsic Lagrangian reference frame (i.e., the wave speeds) is different from the ground-based reference frame. This can be seen clearly in Figure 13(a) where the COSMIC-2 profiles are averaged over boxes in a ground-based reference frame, in comparison to a reference frame that moves with the balloon in Figure 11(d). The latter appears quite similar to the BRO profiles. In fact, the period estimated for the former is closer to 16 days, whereas the intrinsic period that is observed by BRO is closer to 20 days. Often the dispersion curves calculated in the Lagrangian reference frame for different wave types are

530 shown on the same diagrams with satellite derived observations in the Earth-fixed reference frame (i.e., Kiladis et al. (2009), without accounting for these differences. This is an important point to consider when estimating tropical wave signatures from satellite data and interpreting the link between convection, clouds, rain, and tropical weather. Similarly, the difference is also highlighted in the shorter period data from BRO in Figure 11(b) where waves with an intrinsic period of 3–4 day are present. The radiosonde data in the ground-based reference frame in Figure 13(b) is probably capturing the same waves. However, they

535 do not represent the same intrinsic period. This is further complicated due to the likelihood that the data likely contains many wave types. The intrinsic period and wave speed can be significantly overestimated if this assumption is made, also affecting any estimates of momentum flux used to constrain climate models.

The wave analysis is based on dry temperature profiles above 10 km, using the retrieval method based on the assumptions of negligible water vapor and hydrostatic equilibrium (Kursinski et al., 1997). There is an apparent deviation of dry temperature
540   from the true temperature at lower altitudes. With prior information from a first guess model about the temperature and water vapor pressure and their uncertainties, the temperature and moisture information could potentially be retrieved using 1D-VAR methodology (Poli et al., 2002), for example, as implemented in COSMIC Data Analysis and Archive Center(CDAAC) (cdd, 2005). However, as seen in Figure 6, this would involve a more complicated interpretation of the wave structure in the altitudes of interest when the background or first guess model has a significantly different vertical structure, so it is not used here.

545   Very high accuracy positioning is required for balloon-borne RO observations because of the sensitivity to Doppler velocity errors. The higher accuracy positioning yields an additional benefit relative to the single-frequency GNSS receiver in the standard TSEN sensor package provided for all deployed balloons. This precise positioning provides better estimates of the winds and reliable vertical positions that are independent of the pressure measurement, which makes it possible to resolve the Eulerian pressure independently of altitude for the intrinsic phase speed estimation in the spectral analysis of the in situ data
550   (Boccara et al., 2008; Vincent and Hertzog, 2014). This was illustrated in the high precision positioning used in the gravity wave analysis of the stratospheric balloon data from the Antarctic Concordiasi campaign and led to better estimates of momentum flux of high-frequency gravity wave (Zhang et al., 2016). A similar analysis is planned for future Strateole-2 observations.

The COSMIC-2 constellation provides profiles over the tropical oceans operationally for assimilation into numerical weather prediction models. The increased density of the Strateole-2 observations provides potential added value for models. The ob-
555   servations are transmitted via Iridium satellite communication link at 1 hour delays, so the potential exists to provide near real-time observations for improving model initial conditions over the tropical oceans in future campaigns.

8   Conclusions

This work is the culmination of efforts to design and deploy 2nd generation Global Navigation Satellite System (GNSS) receivers for Radio OCcultation (ROC2) onboard equatorial long-duration stratospheric balloons. The Strateole-2 technology
560   demonstration campaign in 2019–2020 was the first time that balloon-borne GNSS RO (BRO) has been used to derive high vertical resolution equatorial wave observations. About 45 temperature profiles were retrieved daily over a period of 17 days, from ~20 km down to a median altitude of 8 km. The BRO technique samples the atmosphere in an orthogonal pattern over a broad area (±400–500 km) along both sides of the flight track, which will be helpful in the future for examining horizontal variations in wave propagation characteristics.

565   For verification, retrieved refractivity and dry temperature profiles were compared with colocated radiosonde observations over Indonesia within 300 km and 1 hour of the observation time. The BRO refractivity profiles show good agreement with radiosondes, given the large horizontal drift of the profile tangent points, within 2 % refractivity and 1 K temperature from flight level to 10 km altitude. Most importantly, the BRO profiles, with vertical resolution better than 500 m, show the same vertical wave structure in the temperature and wave-generated depression of the cold point tropopause as is seen in the radiosonde
570   profiles. Over the duration of the flight over the maritime continent, the mean difference with the ERA5 reanalysis is less than

0.2 % refractivity above 7 km, and the standard deviation is less than 1 %. A systematic bias in comparison with ERA5 from 15 to 20 km is explained by a large-scale Kelvin wave observed in the data that is not adequately resolved or represented in the ERA5 reanalysis. We computed the daily regional mean from the much sparser COSMIC-2 RO profiles to compare to the daily mean BRO profiles and found excellent agreement from balloon flight level down to 8 km altitude, with an RMS difference

575 less than 0.1 % refractivity. Slightly larger differences at 17–18 km are a possible indication that wave variations with less than 3 km wavelength are not resolved as well in the sparser spaceborne RO dataset.

The dominant signal in the individual BRO profile transects, made visible by the consecutive sampling in time and space, is a large-scale Kelvin wave with ∼3–6 km vertical wavelength. The same Kelvin wave is also visible in the COSMIC-2 data, when a new approach is used to bin the COSMIC-2 data following the balloon trajectory, essentially mapping the COSMIC-2

580 observations into the intrinsic reference frame. However, the BRO observations with slightly higher vertical resolution and denser sampling retrieved a higher amplitude temperature variation associated with the wave. The BRO observations present the advantage that the waves are naturally measured in the intrinsic reference frame. After removing the large-scale signal of the Kelvin wave, the BRO observations show wave variations with 2–3 km vertical wavelength that are interpreted to be westward propagating inertia-gravity waves with a 3–4 day period. These results demonstrate the ability to extract fine-vertical

585 scale wave properties continuously in time and space in poorly sampled regions of the globe. The results are promising and indicate that the data will be useful for distinguishing contributions that waves of different scales make to momentum forces for wave driving of the QBO, which is expected to lead to improved QBO representation in models.

We retrieved a short dataset from the Galileo and GLONASS constellations with comparable accuracy to GPS (results not shown here, see ARO dataset in Haase et al., 2021), which demonstrates the feasibility to nearly double the sampling density.

590 Iridium data rates are expected to be high enough to support the continuous transmission of all constellations throughout the entire flight. Five balloons carrying the ROC2 receiver will be deployed to perform RO observations in a follow-on campaign. Exploiting the full dataset and the information available from the directional sampling of the profiles on the north and south sides of the balloon paths will provide opportunities to capture waves over an even broader range of scales.

BRO observations contribute to the larger objectives of the Strateole-2 campaigns that include multiple types of instruments

595 to be flown in the coming years. The high vertical resolution provides new knowledge on fine-vertical scale waves that are un-resolved in global models and provides direct observations of their spatial structure. When combined with other observations such as the Strateole-2 BeCOOL micro-lidar nadir cloud observations, the BRO observations will help determine the relation-ship of upper troposphere waves to the presence of cirrus clouds that can be used for improving model representations of these clouds. They will help quantify global characteristics of waves that determine cold point tropopause temperature variability

600 for use in improving models of stratospheric dehydration. Slow upwelling, rapid transport by penetrating deep convection, thin cirrus formation, and horizontal transport and cooling by waves combine to give the observed variability in water vapor on timescales ranging from very short to decadal. Because stratospheric water vapor plays an important role in the radiative budget of the stratosphere as well as in modulating surface warming, quantifying wave properties in the equatorial region that modulate transport of moisture from the troposphere is essential for improving climate models.

615 **Appendix A: Geometry of Balloon-borne RO**

Figure A1. Schematic diagram of balloon-borne RO geometry with a receiver inside a spherically symmetric atmosphere (shaded). The solid lines connecting the balloon and the GPS satellites represent ray paths of the navigational signal at different times, thicker parts within the neutral atmosphere. Point B on the ray path is symmetric with respect to the tangent point to balloon position A. The bending angle α' is the partial bending angle that accounts only for the bending of the ray path segment AB. Note that the schematic figure is not to scale and the ray path bending is exaggerated for the purpose of visualization and is less than 2°.

The BRO geometry is similar to SRO except that the receiver is within the neutral atmosphere, as shown in Figure A1. The excess phase delay is defined as the difference between the observed propagation time of the signal from the satellite to the receiver and the travel time in a vacuum, multiplied by the speed of light. The excess phase is the integral along the ray path of the refractive index. It is the fundamental observed quantity, expressed in distance units as the carrier phase cycles
620 multiplied by the speed of light, and is typically as much as 100–200 m for BRO. The derivative of the excess phase with time is the excess Doppler shift in the GNSS transmitter carrier frequency, for convenience given in units of speed $(\mathrm{m\,s}^{-1})$.

In a spherically symmetric atmosphere, the ray path bending angle can be derived from the excess Doppler shift (Hajj et al., 2002; Kursinski et al., 1997) using an iterative method, geometric constraints, and Bouger's law for optical refraction (Born and Wolf, 1999; Vorobév and Krasilńikova, 1994)

$$a = n_t \cdot r_t = n_T \cdot r_T \cdot \sin\phi_T = n_R \cdot r_R \cdot \sin\phi_R = n(r) \cdot r \cdot \sin\phi. \tag{A1}$$

Here the impact parameter, a, is constant for a given ray path, and ϕ is the angle between the radius vector, r, and the ray path tangent vector. r_T and r_R refer to the radius vectors of the satellite transmitter and receiver positions, respectively, and r_t is the radius at the tangent point. The result is an estimate of bending angle as a function of ray impact parameter a. The accuracy of the bending angle derived from the excess Doppler is subject to the accuracy of the velocity of the transmitter and receiver (Xie et al., 2008; Muradyan, 2012; Muradyan et al., 2011).

Theoretically, the ray path bending is also described by an integral over radius, r, from the receiver altitude to the altitude of tangent point then to the GPS satellite altitude, in the case of a spherically symmetric atmosphere,

$$\alpha(a) = -2a \int_{r_t}^{r_R} \frac{1}{n} \frac{dn}{dr} \frac{dr}{\sqrt{n^2 r^2 - a^2}} - a \int_{r_R}^{r_T} \frac{1}{n} \frac{dn}{dr} \frac{dr}{\sqrt{n^2 r^2 - a^2}}. \tag{A2}$$

The receiver is low enough that it cannot be considered to be in a vacuum, so the asymmetric geometry requires a correction for the in situ refractivity. It also requires a correction for the refractivity above the receiver for the positive elevation angle segment of the ray path from point B to C in figure A1. The partial bending angle is defined as the difference between the total bending accumulated for the ray path arriving at the receiver from an elevation angle below the horizon (negative elevation angle) minus the positive elevation angle bending (Xie et al., 2008). It corresponds to the accumulated bending from the segment of the ray path below the altitude of the receiver, which is the first term on the right side of Eq. (A2). In Figure A1, this segment of the ray path is between point A and point B, which is symmetric with respect to the tangent point. The partial bending angle α' is then inverted using the Abel transform to retrieve the refractive index profile.

$$n(a) = n_R \cdot \exp\left(\frac{1}{\pi} \int_a^{n_R r_R} \frac{\alpha'(x)\,dx}{\sqrt{x^2 - a^2}}\right) \tag{A3}$$

n_R is the refractive index at the receiver altitude and is determined by in situ measurements from meteorological sensors onboard the same balloon. Finally, the refractive index profile as a function of altitude $n(h)$ is retrieved using the relation $a = nr = n(R_E + h)$, where R_E is the local radius of curvature of the ellipsoidal Earth and h is the altitude above the ellipsoid.

Appendix B: Horizontal Resolution

For each balloon-borne RO profile, the retrieved refractivity is derived from an integrated measurement along the ray path, whose effects are represented as a localized value at the tangent point. One way to define the horizontal resolution is to use the length of the ray path centered at the tangent point that contributes 50 % of the excess phase or bending. Using ray-tracing, we simulated the GNSS signal propagation in the atmosphere for one setting occultation near the equator. Figure B1(a) shows
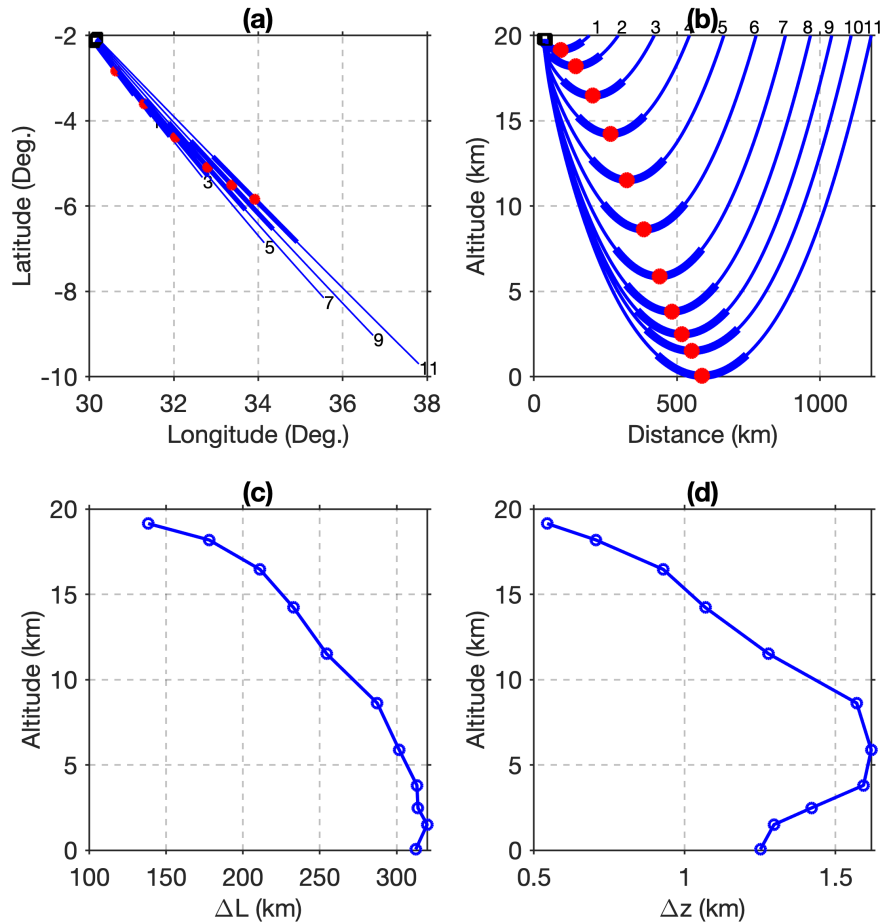
Figure B1. The signal ray paths of one setting occultation in (a) horizontal plan view and (b) vertical cross-section view. The numbers label the ray path traversing the atmosphere from top to bottom with a 300 sec and 150 sec intervals for (a) and (b). The black square marks the position of the balloon that moves a short distance but is shown as nearly stationary in this scale. The red dots denote the tangent point of that ray path and the segments that contribute 50% of the total excess phase are indicated by thicker lines in (a) and (b). (c) and (d) shows the horizontal distance and corresponding altitude range of the ray path segments that contribute 50% of the total excess phase.

the ray paths projected to a horizontal map view and Figure B1(b) shows a vertical cross-section for the segments of the ray paths that traverse the atmosphere below the height of the balloon at 20 km. The thicker segments on the ray path surrounding the tangent points account for 50 % of the total excess phase. The time interval between each ray path shown in panel (b) is 150 s. The horizontal drift of the tangent points (red dots) is clearly seen in these two panels. At this scale, the motion of the balloon during the ∼25 min occultation is imperceptible. The horizontal distance ΔL and corresponding altitude range Δz of this segment provide one way of defining the resolution. In Figure B1(c), ΔL varies from ∼275 km at 10 km height to 170 km at the tropopause at ∼18 km, as Δz varies from ∼1.4 km to to 0.7 km in Figure B1(d).

650

Appendix C: Water Vapor Pressure

When BRO refractivity profiles are compared with other observations such as radiosondes or model output such as the ERA5 reanalysis, the corresponding refractivity needs to be calculated from temperature, pressure, and humidity. In the definition of refractivity in Eq. (1), water vapor pressure p_w is not a direct measurement or model variable. In general, absolute humidity provides a better representation of water vapor content than relative humidity, especially when the water vapor concentration is low. We selected the following formula to calculate water vapor pressure from absolute (specific) humidity:

$$p_w = p \frac{r}{\epsilon + r}, \tag{C1}$$

where r is the water vapor mixing ratio, calculated from specific humidity q [in kg/kg] using $r = q/(1-q)$, and ϵ (R_d/R_w) is the ratio of gas constants for dry air and water vapor, assumed to be 0.622. This formula provides a more accurate estimate of water vapor pressure than other formulas that estimate water vapor pressure from relative humidity based on empirical equations.

Appendix D: IGS Ground Stations

In this study, GPS data from 26 International GNSS Service (IGS) ground stations are used to estimate the regional GPS satellite clock errors in the precise position and phase residual calculation. The selected stations are surrounding the balloon trajectory with a good view of satellites that are potentially in occulting positions relative to the balloon location. The downloaded raw data has a resolution of 30 s, which is sufficient to resolve the variations of satellite clock errors during occultations that typically last 10–20 minutes.
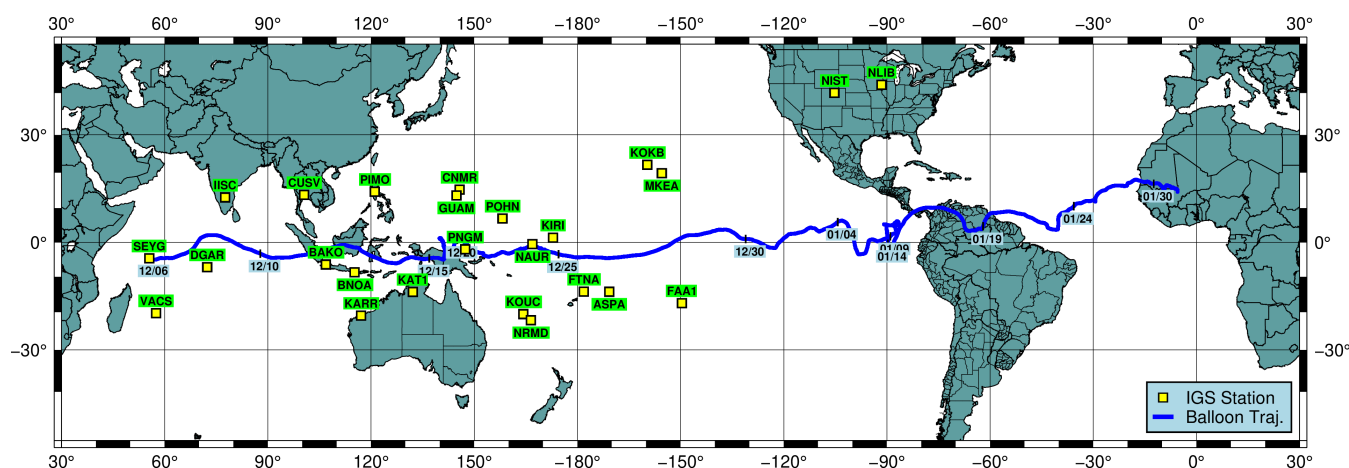
Figure D1. Map of balloon trajectory and selected ground stations from IGS network, that are used in determining the regional GPS satellite clock errors.

Author contributions. JH designed the experiments. JH and BC developed the instrument and carried out the ROC field deployment. AH oversaw the planning and implementation of the larger Strateole-2 campaign and collection of the TSEN data. BC processed and analyzed the data with help from all co-authors. MJA contributed analysis of the TSEN data. BC and JH prepared the manuscript with contributions from all co-authors.

675 *Competing interests.* The authors declare that they have no conflict of interest.

Acknowledgements. Development of the ROC2 instrument and data collection was supported by National Science Foundation (NSF) award AGS-1642650. Infrastructure for the international Strateole-2 balloon campaign was provided by NSF, the French National Centre for Space Studies (CNES), and the French National Centre for Scientific Research Dynamic Meteorology Laboratory (LMD). CNES provided the balloons, flight control systems, flight control gondola "Euros", and Flight Control Center. LMD provided the science payload gondola 680 "Zephyr", which carried the scientific instruments including ROC2, as well as the science data transmission equipment, and provided the associated Mission Control Center (MCC) for monitoring and control of the instruments and the dataset collection. We thank LMD and LATMOS for engineering support in the field. The balloons were released from Mahé international airport, Seychelles, with the local support of the Seychelles Meteorological Authority. We sincerely appreciate their technical and logistical support during the test and deployment of the ROC2 receiver. The ROC2 receivers were built with the assistance of Dave Jabson of Brainstorm Engineering, John Souders and 685 Sean McPeak of SIO/UCSD, and Steven Liang of UCSD. Dr. Stig Syndergaard is acknowledged for providing the original ROSAP ray-tracing model. We acknowledge the support of the National Oceanic and Atmospheric Administration (NOAA) Aircraft Operation Center, in particular, Gabriel Defeo and Jack Parrish, for helping test the ROC2 receiver on the G-IV aircraft. We also acknowledge technical support from Septentrio Inc., Technologic Systems Inc., UNAVCO, and the United States Antarctic Program (USAP) during the development and testing of the ROC2 receiver.

References

Variational Atmospheric Retrieval Scheme (VARS) for GPS Radio Occultation Data, Tech. rep., COSMIC Project Office, University Corporation for Atmospheric Research, 2005.

Andrews, D. G., Holton, J. R., and Leovy, C. B.: Middle Atmosphere Dynamics, 40, Academic Press, 1987.

Anstey, J. A., Banyard, T. P., Butchart, N., Coy, L., Newman, P. A., Osprey, S., and Wright, C.: Quasi-biennial oscillation disrupted by abnormal Southern Hemisphere stratosphere, Earth and Space Science Open Archive, p. 23, https://doi.org/10.1002/essoar.10503358.2, 2020a.

Anstey, J. A., Banyard, T. P., Butchart, N., Coy, L., Newman, P. A., Osprey, S., and Wright, C.: Prospect of increased disruption to the QBO in a changing climate, Earth and Space Science Open Archive, p. 24, https://doi.org/10.1002/essoar.10503358.3, 2020b.

Baldwin, M. P., Gray, L. J., Dunkerton, T. J., Hamilton, K., Haynes, P. H., Randel, W. J., Holton, J. R., Alexander, M. J., Hirota, I., Horinouchi, T., Jones, D. B. A., Kinnersley, J. S., Marquardt, C., Sato, K., and Takahashi, M.: The Quasi-Biennial Oscillation, Rev. Geophys., 39, 179–229, http://dx.doi.org/10.1029/1999RG000073, 2001.

Boccara, G., Hertzog, A., Vincent, R. A., and Vial, F.: Estimation of Gravity Wave Momentum Flux and Phase Speeds from Quasi-Lagrangian Stratospheric Balloon Flights. Part I: Theory and Simulations, J. Atmos. Sci, 65, 3042–3055, https://doi.org/10.1175/2008JAS2709.1, 2008.

Born, M. and Wolf, E.: Principles of optics: electromagnetic theory of propagation, interference and diffraction of light, Cambridge University Press, New York, 7th (expanded) edn., 1999.

Bushell, A. C., Anstey, J. A., Butchart, N., Kawatani, Y., Osprey, S. M., Richter, J. H., Serva, F., Braesicke, P., Cagnazzo, C., Chen, C.-C., Chun, H.-Y., Garcia, R. R., Gray, L. J., Hamilton, K., Kerzenmacher, T., Kim, Y.-H., Lott, F., McLandress, C., Naoe, H., Scinocca, J., Smith, A. K., Stockdale, T. N., Versick, S., Watanabe, S., Yoshida, K., and Yukimoto, S.: Evaluation of the Quasi-Biennial Oscillation in global climate models for the SPARC QBO-initiative, Quarterly Journal of the Royal Meteorological Society, 1, https://doi.org/10.1002/qj.3765, 2020.

Chen, X. M., Chen, S.-H., Haase, J. S., Murphy, B. J., Wang, K.-N., Garrison, J. L., Chen, S. Y., Huang, C. Y., Adhikari, L., and Xie, F.: The Impact of Airborne Radio Occultation Observations on the Simulation of Hurricane Karl (2010), Monthly Weather Review, 146, 329–350, https://doi.org/10.1175/MWR-D-17-0001.1, 2018.

Corcos, M., Hertzog, A., Plougonven, R., and Podglajen, A.: Observation of Gravity Waves at the Tropical Tropopause Using Superpressure Balloons, Journal of Geophysical Research: Atmospheres, 126, e2021JD035 165, https://doi.org/10.1029/2021JD035165, e2021JD035165 2021JD035165, 2021.

Dach, R., Schaer, S., Arnold, D., Kalarus, M. S., Prange, L., Stebler, P., Villiger, A., and Jäggi, A.: CODE final product series for the IGS, https://doi.org/10.7892/boris.75876.4, 2020.

de la Torre, A., Alexander, P., Schmidt, T., Llamedo, P., and Hierro, R.: On the distortions in calculated GW parameters during slanted atmospheric soundings, Atmospheric Measurement Techniques, 11, 1363–1375, https://doi.org/10.5194/amt-11-1363-2018, 2018.

European Centre for Medium-Range Weather Forecasts: ERA5 Reanalysis (0.25 Degree Latitude-Longitude Grid), https://doi.org/10.5065/BH6N-5N20, 2019.

Fjeldbo, G. and Eshleman, V. R.: The atmosphere of mars analyzed by integral inversion of the Mariner IV occultation data, Planetary and Space Science, 16, 1035–1059, https://doi.org/10.1016/0032-0633(68)90020-2, 1968.

Ge, M., Gendt, G., Rothacher, M., Shi, C., and Liu, J.: Resolution of GPS carrier-phase ambiguities in Precise Point Positioning (PPP) with daily observations, Journal of Geodesy, 82, 389–399, https://doi.org/10.1007/s00190-007-0187-4, 2008.

Geng, J., Shi, C., Ge, M., Dodson, A. H., Lou, Y., Zhao, Q., and Liu, J.: Improving the estimation of fractional-cycle biases for ambiguity resolution in precise point positioning, Journal of Geodesy, 86, 579–589, https://doi.org/10.1007/s00190-011-0537-0, 2011.

730 Geng, J., Chen, X., Pan, Y., Mao, S., Li, C., Zhou, J., and Zhang, K.: PRIDE PPP-AR: An Open-Source Software for GPS PPP Ambiguity Resolution, GPS Solut., 23, 1–10, https://doi.org/10.1007/s10291-019-0888-1, 2019.

Haase, J. S., Maldonado-Vargas, J., Rabier, F., Cocquerez, P., Minois, M., Guidard, V., Wyss, P., and Johnson, A. V.: A proof-of-concept balloon-borne Global Positioning System radio occultation profiling instrument for polar studies, Geophysical Research Letters, 39, https://doi.org/10.1029/2011GL049982, l02803, 2012.

735 Haase, J. S., Murphy, B. J., Muradyan, P., Nievinski, F. G., Larson, K. M., Garrison, J. L., and Wang, K.-N.: First results from an airborne GPS radio occultation system for atmospheric profiling, Geophysical Research Letters, 41, 1759–1765, https://doi.org/10.1002/2013GL058681, 2013GL058681, 2014.

Haase, J. S., Alexander, M. J., A. Hertzog, L. K., Deshler, T., Davis, S. M., Plougonven, R., Cocquerez, P., and Venel, S.: Around the world in 84 days, EOS,, 99, https://doi.org/10.1029/2018EO091907, 2018.

740 Haase, J. S., Murphy, M. J., Cao, B., Ralph, F. M., Zheng, M., and Delle Monache, L.: Multi-GNSS Airborne Radio Occultation Observations as a Complement to Dropsondes in Atmospheric River Reconnaissance, Journal of Geophysical Research: Atmospheres, 126, e2021JD034 865, https://doi.org/10.1029/2021JD034865, 2021.

Hajj, G., Kursinski, E., Romans, L., Bertiger, W., and Leroy, S.: A technical description of atmospheric sounding by GPS occultation, Journal of Atmospheric and Solar-Terrestrial Physics, 64, 451–469, https://doi.org/10.1016/S1364-6826(01)00114-6, 2002.

745 Healy, S. B., Haase, J., and Lesne, O.: Abel transform inversion of radio occultation measurements made with a receiver inside the Earth's atmosphere, Annales Geophysicae, 20, 1253–1256, https://doi.org/10.5194/angeo-20-1253-2002, 2002.

Hersbach, H., Bell, B., Berrisford, P., Hirahara, S., Horányi, A., Muñoz-Sabater, J., Nicolas, J., Peubey, C., Radu, R., Schepers, D., Simmons, A., Soci, C., Abdalla, S., Abellan, X., Balsamo, G., Bechtold, P., Biavati, G., Bidlot, J., Bonavita, M., De Chiara, G., Dahlgren, P., Dee, D., Diamantakis, M., Dragani, R., Flemming, J., Forbes, R., Fuentes, M., Geer, A., Haimberger, L., Healy, S., Hogan, R. J.,

750 Hólm, E., Janisková, M., Keeley, S., Laloyaux, P., Lopez, P., Lupu, C., Radnoti, G., de Rosnay, P., Rozum, I., Vamborg, F., Villaume, S., and Thépaut, J.-N.: The ERA5 global reanalysis, Quarterly Journal of the Royal Meteorological Society, 146, 1999–2049, https://doi.org/10.1002/qj.3803, 2020.

Hertzog, A., Boccara, G., Vincent, R. A., Vial, F., and Cocquerez, P.: Estimation of Gravity Wave Momentum Flux and Phase Speeds from Quasi-Lagrangian Stratospheric Balloon Flights. Part II: Results from the Vorcore Campaign in Antarctica, J. Atmos. Sci., 65, 3056–3070,

755 2008.

Ho, S.-P., Anthes, R. A., Ao, C. O., Healy, S., Horanyi, A., Hunt, D., Mannucci, A. J., Pedatella, N., Randel, W. J., Simmons, A., Steiner, A., Xie, F., Yue, X., and Zeng, Z.: The COSMIC/FORMOSAT-3 Radio Occultation Mission after 12 years: Accomplishments, Remaining Challenges, and Potential Impacts of COSMIC-2, Bulletin of the American Meteorological Society, https://doi.org/10.1175/BAMS-D-18-0290.1, 2019.

760 Hoeg, P., H., A., K., G., S., S., Belloul, B., Leitinger, R., and Rothleitner, W.: Derivation of atmospheric properties using a radio occultation technique, Sci. Rep., Tech. rep., Danish Meteorol. Inst., Aalborg, Denmark:, 1996.

Jensen, E. J., Pfister, L., Jordan, D. E., Bui, T. V., Ueyama, R., Singh, H. B., Thornberry, T. D., Rollins, A. W., Gao, R.-S., Fahey, D. W., Rosenlof, K. H., Elkins, J. W., Diskin, G. S., DiGangi, J. P., Lawson, R. P., Woods, S., Atlas, E. L., Rodriguez, M. A. N., Wofsy, S. C.,

Pittman, J., Bardeen, C. G., Toon, O. B., Kindel, B. C., Newman, P. A., McGill, M. J., Hlavka, D. L., Lait, L. R., Schoeberl, M. R.,
765   Bergman, J. W., Selkirk, H. B., Alexander, M. J., Kim, J.-E., Lim, B. H., Stutz, J., and Pfeilsticker, K.: The NASA Airborne Tropical
       Tropopause Experiment: High-Altitude Aircraft Measurements in the Tropical Western Pacific, Bulletin of the American Meteorological
       Society, 98, 129 – 143, https://doi.org/10.1175/BAMS-D-14-00263.1, 2017.

Kawatani, Y. and Hamilton, K.: Weakened stratospheric quasibiennial oscillation driven by increased tropical mean upwelling, Nature, 497,
       478–481, https://doi.org/10.1038/nature12140, 2013.

770   Kiladis, G. N., Wheeler, M. C., Haertel, P. T., Straub, K. H., and Roundy, P. E.: Convectively coupled equatorial waves, Reviews of Geo-
       physics, 47, https://doi.org/10.1029/2008RG000266, 2009.

Kim, J.-E. and Alexander, M. J.: Direct impacts of waves on tropical cold point tropopause temperature, Geophysical Research Letters, 42,
       1584–1592, https://doi.org/10.1002/2014GL062737, 2015.

Kirchengast, G., J., H., and W, P.: The CIRA86aQ_UoG model: An extension of the CIRA-86 monthly tables including humidity tables and
775   a Fortran 95 global moist air climatology model., Tech. Rep. IMG/UoG Techn Rep 8, Eur Space Agency, Paris, France, 1999.

Kursinski, E. R., Hajj, G. A., Schofield, J. T., Linfield, R. P., and Hardy, K. R.: Observing Earth's atmosphere with radio occul-
       tation measurements using the Global Positioning System, Journal of Geophysical Research: Atmospheres, 102, 23 429–23 465,
       https://doi.org/10.1029/97JD01569, 1997.

Lemoine, F. G., Kenyon, S. C., Factor, J. K., Trimmer, R., Pavlis, N. K., Chinn, D. S., Cox, C. M., Klosko, S. M., Luthcke, S. B., Torrence,
780   M. H., Wang, Y. M., Williamson, R. G., Pavlis, E. C., Rapp, R. H., and Olson, T. R.: The Development of the Joint NASA GSFC and
       NIMA Geopotential Model EGM96, Tech. rep., NASA Goddard Space Flight Center, Greenbelt, Maryland, 20771 USA,, 1998.

Lou, Y., Zhang, W., Wang, C., Yao, X., Shi, C., and Liu, J.: The impact of orbital errors on the estimation of satellite clock errors and PPP,
       Advances in Space Research, 54, 1571–1580, https://doi.org/10.1016/j.asr.2014.06.012, 2014.

Muradyan, P.: Profiling the atmosphere with the airborne GPS radio occultation technique using open-loop tracking, Ph.D. thesis, Purdue
785   University, West Lafayette, IN, U.S.A., 2012.

Muradyan, P., Haase, J. S., Xie, F., Garrison, J. L., and Voo, J.: GPS/INS navigation precision and its effect on airborne radio occultation
       retrieval accuracy, GPS Solutions, 15, 207–218, https://doi.org/10.1007/s10291-010-0183-7, 2011.

Murphy, B. J.: Profiling the Moisture Environment of Developing Tropical Storms using Airborne Radio Occultation, Ph.D. thesis, Purdue
       University, 2015.

790   Murphy, B. J., Haase, J. S., Muradyan, P., Garrison, J. L., and Wang, K.-N.: Airborne GPS radio occultation refractivity profiles observed
       in tropical storm environments, Journal of Geophysical Research: Atmospheres, 120, 1690–1709, https://doi.org/10.1002/2014JD022931,
       2014JD022931, 2015.

Newman, P. A., Coy, L., Pawson, S., and Lait, L. R.: The anomalous change in the QBO in 2015–2016, Geophysical Research Letters, 43,
       8791–8797, https://doi.org/10.1002/2016GL070373, 2016.

795   Podglajen, A., Hertzog, A., Plougonven, R., and Legras, B.: Lagrangian temperature and vertical velocity fluctuations due to gravity waves
       in the lower stratosphere, Geophysical Research Letters, 43, 3543–3553, https://doi.org/10.1002/2016GL068148, 2016.

Poli, P., Joiner, J., and Kursinski, E. R.: 1DVAR analysis of temperature and humidity using GPS radio occultation refractivity data, Journal
       of Geophysical Research: Atmospheres, 107, ACL 14–1–ACL 14–20, https://doi.org/10.1029/2001JD000935, 2002.

Rabier, F., Bouchard, A., Brun, E., Doerenbecher, A., Guedj, S., Guidard, V., Karbou, F., Peuch, V.-H., Amraoui, L. E., Puech, D., Genthon,
800   C., Picard, G., Town, M., Hertzog, A., Vial, F., Cocquerez, P., Cohn, S. A., Hock, T., Fox, J., Cole, H., Parsons, D., Powers, J., Romberg,
       K., VanAndel, J., Deshler, T., Mercer, J., Haase, J. S., Avallone, L., Kalnajs, L., Mechoso, C. R., Tangborn, A., Pellegrini, A., Frenot, Y.,

Thépaut, J.-N., McNally, A., Balsamo, G., and Steinle, P.: The Concordiasi Project in Antarctica, Bulletin of the American Meteorological Society, 91, 69 – 86, https://doi.org/10.1175/2009BAMS2764.1, 2010.

Ralph, F. M., Cannon, F., Tallapragada, V., Davis, C. A., Doyle, J. D., Pappenberger, F., Subramanian, A., Wilson, A. M., Lavers, D. A.,
805   Reynolds, C. A., Haase, J. S., Centurioni, L., Ingleby, B., Rutz, J. J., Cordeira, J. M., Zheng, M., Hecht, C., Kawzenuk, B., and Monache, L. D.: West Coast Forecast Challenges and Development of Atmospheric River Reconnaissance, Bulletin of the American Meteorological Society, 101, E1357 – E1377, https://doi.org/10.1175/BAMS-D-19-0183.1, 2020.

Randel, W. J., Wu, F., and Rivera Ríos, W.: Thermal variability of the tropical tropopause region derived from GPS/MET observations, Journal of Geophysical Research: Atmospheres, 108, ACL 7–1–ACL 7–12, https://doi.org/10.1029/2002JD002595, 2003.

810   Ravetta, F., Vincent Mariage, Emmanuel Brousse, Eric d´Almeida, Frédéric Ferreira , Jacques Pelon, and Stéphane Victori: BeCOOL: A Balloon-Borne Microlidar System Designed for Cirrus and Convective Overshoot Monitoring, EPJ Web Conf., 237, 07 003, https://doi.org/10.1051/epjconf/202023707003, 2020.

Richter, J. H., Butchart, N., Kawatani, Y., Bushell, A. C., Holt, L., Serva, F., Anstey, J., Simpson, I. R., Osprey, S., Hamilton, K., Braesicke, P., Cagnazzo, C., Chen, C.-C., Garcia, R. R., Gray, L. J., Kerzenmacher, T., Lott, F., McLandress, C., Naoe, H., Scinocca, J., Stockdale,
815   T. N., Versick, S., Watanabe, S., Yoshida, K., and Yukimoto, S.: Response of the Quasi-Biennial Oscillation to a warming climate in global climate models, Quarterly Journal of the Royal Meteorological Society, 1, https://doi.org/10.1002/qj.3749, 2020.

Rüeger, J.: Refractive index formulae for electronic distance measurements with radio and millimetre waves, Rep. Unisurv Rep, 109, 758–766, 2002.

Saastamoinen, J.: Atmospheric Correction for the Troposphere and Stratosphere in Radio Ranging Satellites, pp. 247–251, American Geo-
820   physical Union (AGU), https://doi.org/10.1029/GM015p0247, 1972.

Sato, K. and Dunkerton, T. J.: Estimates of momentum flux associated with equatorial Kelvin and gravity waves, Journal of Geophysical Research: Atmospheres, 102, 26 247–26 261, https://doi.org/10.1029/96JD02514, 1997.

Scherllin-Pirscher, B., Steiner, A. K., Anthes, R. A., Alexander, M. J., Alexander, S. P., Biondi, R., Birner, T., Kim, J., Randel, W. J., Son, S.-W., Tsuda, T., and Zeng, Z.: Tropical Temperature Variability in the UTLS: New Insights from GPS Radio Occultation Observations,
825   Journal of Climate, 34, 2813–2838, https://doi.org/10.1175/jcli-d-20-0385.1, 2021.

Schreiner, W., Weiss, J., Anthes, R., Braun, J., Chu, V., Fong, J., Hunt, D., Kuo, Y.-H., Meehan, T., Serafino, W., Sjoberg, J., Sokolovskiy, S., Talaat, E., Wee, T., and Zeng, Z.: COSMIC-2 Radio Occultation Constellation: First Results, Geophysical Research Letters, 47, e2019GL086 841, https://doi.org/10.1029/2019GL086841, e2019GL086841 2019GL086841, 2020.

Shi, C., Zhao, Q., Geng, J., Lou, Y., Ge, M., and Liu, J.: Recent development of PANDA software in GNSS data processing, in: International
830   Conference on Earth Observation Data Processing and Analysis (ICEODPA), edited by Li, D., Gong, J., and Wu, H., vol. 7285, pp. 558 – 566, International Society for Optics and Photonics, SPIE, https://doi.org/10.1117/12.816261, 2008.

Simmons, A. J. and Burridge, D. M.: An Energy and Angular-Momentum Conserving Vertical Finite-Difference Scheme and Hybrid Vertical Coordinates, Monthly Weather Review, 109(4), 758–766, 1981.

Syndergaard, S.: Modeling the impact of the Earth's oblateness on the retrieval of temperature and pressure profiles from limb sounding,
835   Journal of Atmospheric and Solar-Terrestrial Physics, 60, 171 – 180, https://doi.org/10.1016/S1364-6826(97)00056-4, 1998.

Trenberth, K. E., Berry, J. C., and Buja, L. E.: Vertical Interpolation and Truncation of Model-coordinate Data (No. NCAR/TN-396+STR), Tech. rep., University Corporation for Atmospheric Research, https://doi.org/10.5065/D6HX19NH, 1993.

Tsuda, T., Murayama, Y., Wiryosumarto, H., Harijono, W. B., , and Kato, S.: Radiosonde observations of equatorial atmosphere dynamics over Indonesia: 1. Equatorial waves and diurnal tides, Journal of Geophysical Research: Atmospheres, 99, 10 491–10 505, https://doi.org/10.1029/94JD00355, 1994.

Tsuda, T., Nishida, M., Rocken, C., and Ware, R. H.: A global morphology of gravity wave activity in the stratosphere reveald by the GPS occultationi data (GPS/MET), J. Geophys. Res., 105, 7257–7273, 2000.

Vincent, R. A. and Alexander, M. J.: Balloon-Borne Observations of Short Vertical Wavelength Gravity Waves and Interaction With QBO Winds, Journal of Geophysical Research: Atmospheres, 125, https://doi.org/10.1029/2020JD032779, 2020.

Vincent, R. A. and Hertzog, A.: The response of superpressure balloons to gravity wave motions, Atmospheric Measurement Techniques, 7, 1043–1055, https://doi.org/10.5194/amt-7-1043-2014, 2014.

Vorobév, V. V. and Krasilńikova, T. G.: Estimation of the accuracy of the atmospheric refractive index recovery from Doppler shift measurements at frequencies used in the NAVSTAR system, Physics of The Atmosphere and Ocean, 29, 602–609, 1994.

Xie, F., Haase, J. S., and Syndergaard, S.: Profiling the Atmosphere Using the Airborne GPS Radio Occultation Technique: A Sensitivity Study, IEEE Transactions on Geoscience and Remote Sensing, 46, 3424–3435, https://doi.org/10.1109/TGRS.2008.2004713, 2008.

Zeng, Z., Ho, S.-P., Sokolovskiy, S., and Kuo, Y.-H.: Structural evolution of the Madden-Julian Oscillation from COSMIC radio occultation data, Journal of Geophysical Research: Atmospheres, 117, https://doi.org/10.1029/2012JD017685, 2012.

Zhang, W., Haase, J. S., Hertzog, A., Lou, Y., and Vincent, R.: Improvement of stratospheric balloon GPS positioning and the impact on gravity wave parameter estimation for the Concordiasi campaign in Antarctica, Journal of Geophysical Research: Atmospheres, 121, 9977–9997, https://doi.org/10.1002/2015JD024596, 2016.

List of Figures